The Astrophysical Journal, 887:91 (17pp), 2019 December 10 https://doi.org/10.3847/1538-4357/ab53d9


# Chemical Abundances along the 1G Sequence of the Chromosome Maps: The Globular Cluster NGC 3201*

A. F. Marino[1,2], A. P. Milone[1], A. Sills[3], D. Yong[4], A. Renzini[5], L. R. Bedin[5], G. Cordoni[1], F. D'Antona[6], H. Jerjen[4], A. Karakas[7], E. Lagioia[1], G. Piotto[1], and M. Tailo[1]
[1] Dipartimento di Fisica e Astronomia "Galileo Galilei"—Univ. di Padova, Vicolo dell'Osservatorio 3, Padova, I-35122, Italy; anna.marino@unipd.it
[2] Centro di Ateneo di Studi e Attivita' Spaziali "Giuseppe Colombo"—CISAS, Via Venezia 15, Padova, I-35131, Italy
[3] Department of Physics & Astronomy, McMaster University, 1280 Main Street West, Hamilton, ON, L8S 4M1, Canada
[4] Research School of Astronomy & Astrophysics, Australian National University, Canberra, ACT 2611, Australia
[5] Istituto Nazionale di Astrofisica—Osservatorio Astronomico di Padova, Vicolo dell'Osservatorio 5, Padova, I-35122, Italy
[6] Istituto Nazionale di Astrofisica—Osservatorio Astronomico di Roma, Via Frascati 33, I-00040 Monteporzio Catone, Roma, Italy
[7] School of Physics & Astronomy, Monash University, Clayton, VIC 3800, Australia
*Received 2019 August 29; revised 2019 October 3; accepted 2019 October 4; published 2019 December 13*

## Abstract

The *Hubble Space Telescope* (*HST*) UV Legacy Survey of Galactic Globular Clusters (GCs) has investigated multiple stellar populations by means of the "chromosome map" (ChM) diagnostic tool that maximizes the separation between stars with different chemical compositions. One of the most challenging features revealed by ChM analysis is the apparent inhomogeneity among stars belonging to the first population, a phenomenon largely attributed to He variations. However, this explanation is not supported by uniformity in the *p*-capture elements of these stars. The *HST* survey has revealed that the GC NGC 3201 shows exceptionally wide coverage in the $\Delta_{\rm F275W,F814W}$ parameter of the ChM. We present a chemical abundance analysis of 24 elements in 18 giants belonging to the first population of this GC and having a wide range in $\Delta_{\rm F275W,F814W}$. As far as the *p*-capture elements are concerned, the chemical abundances are typical of first-generation (1G) stars, as expected from the location of our targets in the ChM. Based on radial velocities and chemical abundance arguments, we find that the three stars with the lowest $\Delta_{\rm F275W,F814W}$ values are binary candidates. This suggests that at least those stars could be explained with binarity. These results are consistent with evidence inferred from multiband photometry that evolved blue stragglers (BSs) populate the bluest part of the 1G sequence in the ChM. The remaining 15 spectroscopic targets show a small range in the overall metallicity by ∼0.10 dex, with stars at higher $\Delta_{\rm F275W,F814W}$ values having higher absolute abundances. We suggest that a small variation in metals and binarity governs the color spread of the 1G in the ChM and that evolved BSs contribute to the bluest tail of the 1G sequence.

*Unified Astronomy Thesaurus concepts:* Population II stars (1284); Stellar populations (1622); Globular star clusters (656); Hertzsprung Russell diagram (725); Chemical abundances (224)

*Supporting material:* machine-readable table

## 1. Introduction

The presence of multiple stellar populations in globular clusters (GCs) is a well-assessed fact. Chemical abundance variations within stars in a given GC have been known for many years now, with some of the earliest studies including Popper (1947), Harding (1962), Osborn (1971), and Cohen (1978). More recently, different stellar populations have been detected through multiple sequences along the color–magnitude diagram (CMD; e.g., Milone et al. 2012a). The photometrically observed multiple sequences are associated with variations in chemical elements involved in hot H burning (light elements, CNONa; see Marino et al. 2008; Yong et al. 2008, for the earliest studies on this issue). One stellar population, usually considered the first population (or generation), is chemically similar to field halo stars, while the other populations display various degrees of enrichment in He/N/Na, depletion in C, and depletion of O with respect to the first population, as opposite to the $\alpha$-enhancement typical in halo field stars (e.g., Carretta et al. 2009; Gratton et al. 2012).

On top of this typical observed pattern, the recent analysis of UV high-precision data from the *Hubble Space Telescope* (*HST*) has revealed an even more complex picture (Milone et al. 2015, 2017). All of the GCs exhibit two main discrete groups of first-generation (1G) and second-generation (2G) stars along the "chromosome maps" (ChMs) that constitute the most effective and successful diagnostic tool to isolate the different populations of stars hosted in a GC. These sort of two-color photometric diagrams, constructed by combining multi-filter *HST* images in $m_{\rm F275W}$, $m_{\rm F336W}$, $m_{\rm F438W}$, and $m_{\rm F814W}$, are highly sensitive to the chemistry of the different stellar populations. On a typical ChM plane, $\Delta_{C\ \rm F275W,F336W,F438W}$ versus $\Delta_{\rm F275W,F814W}$,[8] all of the observed GCs display a typical ChM shape, with a different number of seemingly discrete groups appearing along the main pattern that are associated with distinct stellar populations. By combining spectroscopy and photometry, we find that 1G stars on the ChMs with low $\Delta_{C\ \rm F275W,F336W,F438W}$ values share the same chemical composition as halo field stars at the same metallicity, while 2G stars are enhanced in He, N, and Na and depleted in C and O (Marino et al. 2019).

* Based on observations collected at the European Southern Observatory under ESO program 0101.D-0113(A) and the NASA/ESA *Hubble Space Telescope*, obtained at the Space Telescope Science Institute, which is operated by AURA, Inc., under NASA contract NAS 5-26555.

[8] See Section 2. A detailed definition of $\Delta_{\rm F275W,F814W}$ and $\Delta_{C\ \rm F275W,F336W,F438W}$ can be found in Milone et al. (2015, 2017).

The ChMs exhibit a variety of morphologies in terms of both the number of stellar populations and the shape and extension. Milone et al. (2017) subdivided 57 analyzed maps in two main groups: (i) Type I GCs having a single ChM pattern, with a 1G and two or more 2G populations, and (ii) Type II GCs displaying multiple ChMs, with minor populations located on red additional ChMs. While we refer to Marino et al. (2019) for a detailed chemical characterization of these two main classes of maps, here we just recall that the additional red stellar populations in Type II GCs are enhanced in metallicity and (in some cases) in the elements produced via slow neutron-capture reactions (*s*-elements; e.g., Yong & Grundahl 2008; Marino et al. 2009, 2015).

Besides being a powerful tool to explore the multiple stellar population phenomenon, ChMs provide fundamental information that can shed light on how GCs formed and evolved, which might be hidden in the 1G stars themselves. Indeed, one of the most interesting features observed on the ChMs is perhaps the apparent chemical inhomogeneity within the 1G population. Indeed, the 1G sequence on the ChM is either elongated or bimodal, thus indicating that its stars are not consistent with a simple stellar population. Milone et al. (2015, 2018) and D'Antona et al. (2016) suggested that either a relatively large variation in He, even by $\Delta Y \sim 0.10$, or a small variation in metallicity, by ∼0.10 dex, within 1G stars could reproduce the morphology of the 1G sequence on the map. The homogeneity in the light elements among these stars observed in the ChM of many GCs (Marino et al. 2019; see also Cabrera-Ziri et al. 2019) suggests that, if He is responsible for the elongated distribution of 1G stars on the ChM, a nucleosynthesis process occurred that changed the He content but left untouched the elements involved in the standard H burning, such as C and N (see discussion in Milone et al. 2018). As we are not aware of the existence of such a mechanism, a small variation in metallicity among 1G stars might be a more plausible solution (Marino et al. 2019).

An internal variation in helium among 1G stars seems to not be supported by a recent analysis of horizontal branch stars in M3 (Tailo et al. 2019). The fact that the first population on the maps is inconsistent with one single group poses serious challenges to our current understanding of multiple stellar populations. The possibility that 1G stars have an internal spread in the overall metallicity would suggest that supernovae (SNe) played a role in the star formation history of most GCs and that these stellar systems have been able to retain a small amount of material polluted by the SNe. In such a case, either a fraction of the 1G could be formed from material polluted from a previous generation of stars, thus indicating that only a fraction of 1G stars constitute the real primordial stellar generation, making the mass-budget problem even more dramatic; or the interstellar medium from which 1G stars formed was inhomogeneous. In contrast, the possibility that the 1G has an internal spread in helium (but constant C, N, O, and Fe) could be indicative of some still-unknown mechanism that occurs in GC stars only, possibly an accretion phenomenon in the pre-main-sequence phase.

In this work, we provide a high-resolution spectroscopic abundance analysis of 1G stars as selected from the ChM in the GC NGC 3201. This cluster, displaying a well-elongated 1G population on the ChM, is an ideal target for an in-depth investigation of the chemical abundance pattern within 1G stars. Although its ChM does not show evidence of additional stellar populations on the red side, as in Type II GCs, Dias et al. (2018) found multiple (anti)correlations in light elements, similar to those observed in some of the Type II clusters, such as M22 (Marino et al. 2009). The layout of this paper is as follows. Section 2 presents the photometric and spectroscopic data, Section 3 describes how we derive atmospheric parameters, the chemical abundance analysis is presented in Section 4, Sections 5–7 discuss our results, and the results are summarized in Section 8.

## 2. Data

### 2.1. The Photometric Data Set: The ChM of NGC 3201

The photometric data used in this study come from the *HST* UV Legacy Survey, which investigated multiple stellar populations in GCs (GO-13297; Piotto et al. 2015). Details on the images analyzed and the data reduction can be found in Piotto et al. (2015) and Milone et al. (2017). The photometry has been corrected for differential reddening effects as in Milone et al. (2012b).

Milone et al. (2017) analyzed the ChMs of 57 GCs. While we refer to Milone et al. (2015, 2017) for a detailed discussion on how to construct these photometric diagrams, for the convenience of the reader, we restate here their Equations (1) and (2). Hence, $\Delta_{\rm F275W,F814W}$ and $\Delta_{C\ \rm F275W,F336W,F438W}$ are defined as

$$\Delta_{\rm F275W,F814W} = W_{\rm F275W,F814W}\frac{X - X_{\rm fiducial\ R}}{X_{\rm fiducial\ R} - X_{\rm fiducial\ B}}, \quad (1)$$

$$\Delta_{C\ \rm F275W,F336W,F438W} = W_{\rm C\ F275W,F336W,F438W}\frac{Y_{\rm fiducial\ R} - Y}{Y_{\rm fiducial\ R} - Y_{\rm fiducial\ B}}, \quad (2)$$

where $X = (m_{\rm F275W} - m_{\rm F814W})$, $Y = C_{\rm F275W,F336W,F438W}$, with the latter being an index sensitive to N abundances, and "fiducial R" and "fiducial B" correspond to the red and blue fiducial lines involved in the construction of the ChM.

The analysis of the NGC 3201 ChM revealed that this cluster covers a large range along the $\Delta_{\rm F275W,F814W}$ axis, which is not consistent with the assumed chemical homogeneity of the 1G (see their Figure 4 and our Figure 1).

### 2.2. The Spectroscopic Data Set

Our spectroscopic data have been acquired using the FLAMES Ultraviolet and Visual Echelle Spectrograph (FLAMES-UVES; Pasquini et al. 2000) on the European Southern Observatory's (ESO) Very Large Telescope (VLT) through program 0101.D-0113(A). The observations were taken in the standard RED580 setup, which has a wavelength coverage of 4726–6835 Å and a resolution $R \sim 47{,}000$ (Dekker et al. 2000).

Spectra are based on $5 \times 2775$ s exposures for the seven brightest stars in our sample with $V$ mag between ∼13.5 and ∼14.5 and $23 \times 2775$ s for the three faintest ones with $V > 15$. Stars with intermediate mag have $11 \times 2775$ or $12 \times 2775$ s exposures on them (see Table 1). Data were reduced using the FLAMES-UVES pipelines within the EsoReflex interface[9] (Ballester et al. 2000), including bias subtraction, flat-field correction, wavelength calibration, sky subtraction, and spectral rectification. Once individual spectra were reduced, the telluric

[9] https://www.eso.org/sci/software/esoreflex/

**Table 1**
Coordinates, Photometric Information (Including the Location on the ChM), and RVs, with Associated rms from the Number of Exposures and Maximum Time between Observations (Time Interval)

| ID | R.A. J2000 | Decl. J2000 | $V$ (mag) | $\Delta_{F275W,F814W}$ (mag) | $\Delta_{C\ F275W,F336W,F438W}$ (mag) | RV (km s$^{-1}$) | rms$_{RV}$ (km s$^{-1}$) | No. | Time Interval |
|---|---|---|---|---|---|---|---|---|---|
| 150 | 10:17:31.515 | −46:24:34.66 | 14.007 | −0.112 | 0.024 | 490.8 | 0.22 | 5 | 2 months |
| 160 | 10:17:28.083 | −46:24:33.71 | 14.323 | −0.143 | 0.033 | 493.0 | 0.23 | 5 | 2 months |
| 32 | 10:17:33.746 | −46:25:46.50 | 14.577 | −0.103 | 0.001 | 498.6 | 0.14 | 5 | 2 months |
| 69 | 10:17:38.395 | −46:25:29.28 | 14.542 | −0.155 | 0.012 | 493.1 | 0.17 | 5 | 2 months |
| 58 | 10:17:40.771 | −46:24:44.87 | 13.649 | 0.036 | −0.001 | 498.1 | 0.19 | 5 | 2 months |
| 91 | 10:17:32.111 | −46:25:09.95 | 14.165 | −0.166 | 0.037 | 493.5 | 0.18 | 5 | 2 months |
| 40 | 10:17:29.962 | −46:25:30.57 | 13.821 | −0.081 | 0.004 | 496.8 | 0.21 | 5 | 2 months |
| 147 | 10:17:33.391 | −46:24:25.34 | 14.794 | 0.078 | 0.003 | 493.6 | 0.20 | 12 | 8 months |
| 149 | 10:17:32.115 | −46:24:24.49 | 14.633 | −0.275 | 0.094 | 495.2 | 0.11 | 11 | 3 days |
| 14 | 10:17:41.299 | −46:25:43.50 | 14.674 | −0.083 | 0.008 | 496.0 | 0.20 | 12 | 7 months |
| 158 | 10:17:28.360 | −46:24:03.89 | 14.936 | −0.133 | 0.034 | 494.0 | 0.08 | 11 | 3 days |
| 15 | 10:17:41.161 | −46:25:33.81 | 14.684 | −0.033 | 0.004 | 497.7 | 0.09 | 11 | 3 days |
| 27 | 10:17:36.395 | −46:25:49.35 | 14.732 | 0.003 | −0.014 | 492.5 | 0.08 | 11 | 3 days |
| 33 | 10:17:33.501 | −46:25:30.71 | 15.397 | −0.123 | 0.060 | 492.0 | 0.24 | 23 | 8 months |
| 67 | 10:17:39.149 | −46:25:19.59 | 15.419 | −0.199 | 0.080 | 496.4 | 0.76 | 23 | 8 months |
| 82 | 10:17:35.886 | −46:25:21.01 | 14.685 | 0.004 | −0.020 | 492.6 | 0.19 | 12 | 7 months |
| 93 | 10:17:31.507 | −46:24:58.17 | 14.574 | −0.217 | 0.086 | 506.8 | 0.55 | 12 | 7 months |
| 98 | 10:17:30.035 | −46:25:00.41 | 15.350 | −0.180 | 0.081 | 493.9 | 0.26 | 23 | 8 months |

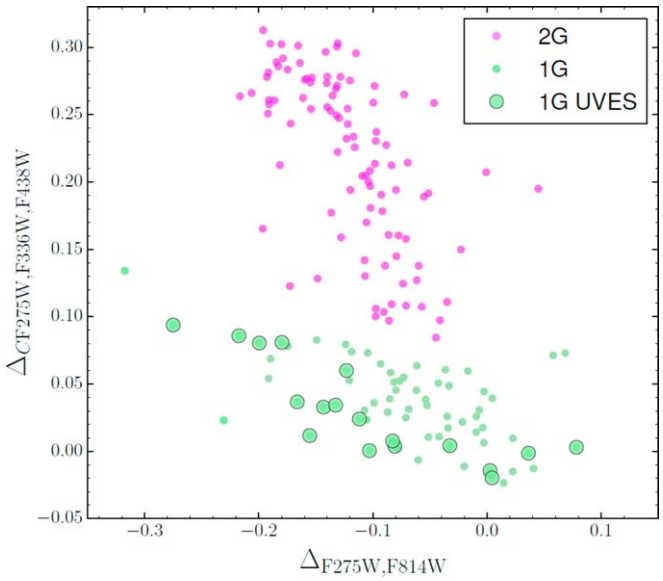


**Figure 1.** The ChM of NGC 3201 from Milone et al. (2017). Stars in green and magenta represent 1G and 2G stars, respectively, as defined by Milone and coworkers. Our 18 spectroscopic UVES targets are all located in the 1G region and highlighted as larger filled circles.

subtraction was performed using the ESO MOLECFIT tool (Kausch et al. 2014; Smette et al. 2014).

Radial velocities (RVs) were derived using the IRAF@FXCOR task, which cross-correlates the object spectrum with a template. For the template, we used a synthetic spectrum obtained through MOOG[10] (version 2014 June; Sneden 1973), computed with a model stellar atmosphere interpolated from the Castelli & Kurucz (2004) grid, adopting parameters (effective temperature/surface gravity/microturbulence/metallicity) = ($T_{\rm eff}$/log $g$/$\xi_{\rm t}$/[A/H]) = (4900 K/2.0/2.0 km s$^{-1}$/−1.50). Each spectrum was corrected to the rest-frame system, and observed RVs were then corrected to the heliocentric system. The mean RVs, together with the associated rms obtained from the average of individual exposures, are listed in Table 1. Since NGC 3201 has a distinct high RV, we can safely assume that all 18 of the observed stars are cluster members. The final mean heliocentric RV for our NGC 3201 giants is $\langle {\rm RV} \rangle = +495.3 \pm 0.9$ km s$^{-1}$ ($\sigma = 3.7$ km s$^{-1}$), which lies within 1$\sigma$ of the literature value of $\langle {\rm RV} \rangle = +494.0 \pm 0.2$ km s$^{-1}$ listed in the Harris catalog (Harris 2010).

Finally, the individual exposures for each star have been coadded. The typical signal-to-noise ratio (S/N) for the combined spectra around the [O I] $\lambda$6300 line ranges from S/N $\sim$ 120 to $\sim$170, depending on the brightness of the star and the number of exposures. The list of observed giants in NGC 3201 is reported in Table 1, together with coordinates, photometric information, RVs, and number of exposures.

## 3. Model Atmospheres

The relatively high resolution and large spectral coverage of our spectra allowed a fully spectroscopic estimate of the stellar parameters, $T_{\rm eff}$, log $g$, [A/H], and $\xi_{\rm t}$. Hence, we determined $T_{\rm eff}$ by imposing the excitation potential (EP) equilibrium of the Fe I lines and gravity with the ionization equilibrium between the Fe I and Fe II lines. Note that for log $g$, we impose Fe II abundances that are 0.05–0.07 dex higher than the Fe I ones to adjust for non-local thermodynamic equilibrium (non-LTE) effects (Bergemann et al. 2012; Lind et al. 2012). This difference is justified by the non-LTE corrections to Fe I and Fe II derived for stars 69 and 82 (see Section 7). The final Fe abundances are based on Fe I, for which we have more available lines. For this analysis, $\xi_{\rm t}$ was set to minimize any dependence of Fe I abundances as a function of equivalent width (EW).

As an independent test of our results, we also derived atmospheric parameters from our *HST* photometry (see Section 2.1). For that purpose, the $m_{\rm F438W}$ and $m_{\rm F606W}$ magnitudes have been converted to $B$ and $V$ (Anderson et al. 2008), which we then used to estimate temperatures from the Alonso et al. (1999) color–temperature calibrations, assuming a

[10] http://www.as.utexas.edu/~chris/moog.html

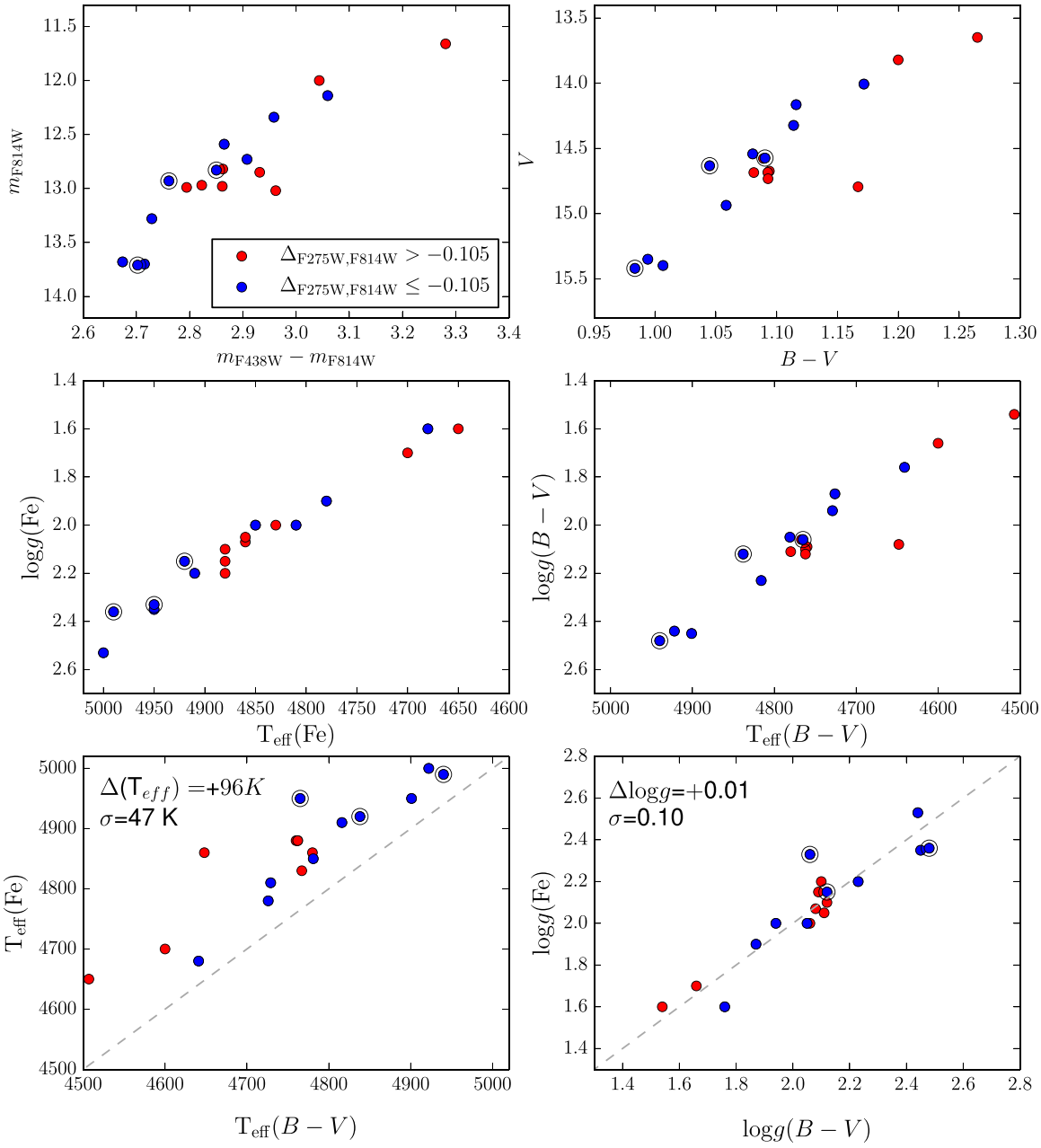


**Figure 2.** Top panels: CMDs from *HST* photometry. On the left, we display the $m_{F814W}$ vs. $m_{F438W} - m_{F814W}$ CMD, while on the right, we show the $V$ –$(B - V)$ CMD with magnitudes obtained from transforming the original *HST* magnitudes (details in Section 2.1). Middle panels: log $g$ vs. $T_{eff}$ as obtained from the Fe lines (left) and $(B - V)$ color (right). Bottom panels: comparison between spectroscopically and photometrically derived parameters $T_{eff}$ and log $g$. The dashed line represents perfect agreement. We label the mean difference and rms among the two sets of parameters. In all panels, blue and red dots represent stars with $\Delta_{F275W,F814W} \leqslant 0.105$ and $\Delta_{F275W,F814W} > -0.105$, respectively.

mean $E(B - V) = 0.24$ and $[A/H] = -1.54$ dex. Surface gravities were then obtained from the apparent $V$ magnitudes, the photometric $T_{eff}$, bolometric corrections from Alonso et al. (1999), the apparent distance modulus of $(m - M)_V = 14.20$ (Harris 2010), and a stellar mass of 0.70 $M_\odot$. Once $T_{eff}$ and log $g$ have been fixed from photometry, we derive $\xi_t$ from the Fe I lines as explained above.

The top panels of Figure 2 show the spectroscopic targets on the *HST* (left) and $V - (B - V)$ (right) CMDs, with stars colored blue and red for $\Delta_{F275W,F814W} \leqslant -0.105$ and $\Delta_{F275W,F814W} > -0.105$, respectively. The small color offset suggests that, at a given luminosity, the blue stars might be slightly hotter. Our adopted log $g$–$T_{eff}$ values that are completely independent from photometry do not show significant evidence for such a trend (middle left panel), which might be slightly more visible in the photometric log $g$–$T_{eff}$ plane (middle right panel). Our internal errors in $T_{eff}$ are probably larger than the expected difference between bluer and redder stars.

To have an estimate of the internal errors associated with our adopted parameters, we compare the $T_{eff}$/log $g$ from Fe lines with those derived from the $(B - V)$ colors in the bottom panels of Figure 2. We obtain $\Delta T_{eff} = T_{effFe\ lines}$–$T_{eff(B-V))} = +96$ K (rms = 47 K) and $\Delta \log g =$ log $g_{Fe\ lines}$–log $g_{(B-V)} = +0.01$ (rms = 0.10). This comparison suggests that the spectroscopic $T_{eff}$ scale is systematically higher by ∼100 K (see bottom left panel), but the internal errors are smaller, comparable with the

**Table 2**
Adopted Atmospheric Parameters Derived from Spectroscopy and the Corresponding Fe I and Fe II Abundances (with the Associated $\sigma$ and Number of Spectral Lines)

| ID | $T_{\rm eff}$ (K) | log $g$ (cgs) | [A/H] (dex) | $\xi_t$ (km s$^{-1}$) | log $\epsilon$(Fe I) dex | $\sigma_{\rm Fe\,I}$ | No.$_{\rm Fe\,I}$ | log $\epsilon$(Fe II) dex | $\sigma_{\rm Fe\,II}$ | No. | $T_{\rm effphotometry}$ (K) | log $g_{\rm photometry}$ (cgs) |
|---|---|---|---|---|---|---|---|---|---|---|---|---|
| 150 | 4680 | 1.60 | −1.55 | 1.53 | 5.95 | 0.09 | 128 | 6.01 | 0.08 | 12 | 4641 | 1.76 |
| 160 | 4810 | 2.00 | −1.48 | 1.48 | 6.02 | 0.09 | 125 | 6.08 | 0.07 | 13 | 4729 | 1.94 |
| 32 | 4830 | 2.00 | −1.46 | 1.44 | 6.04 | 0.11 | 131 | 6.10 | 0.08 | 12 | 4767 | 2.06 |
| 69 | 4850 | 2.00 | −1.55 | 1.48 | 5.95 | 0.09 | 119 | 6.00 | 0.07 | 12 | 4781 | 2.05 |
| 58 | 4650 | 1.60 | −1.44 | 1.64 | 6.06 | 0.09 | 133 | 6.14 | 0.05 | 13 | 4507 | 1.54 |
| 91 | 4780 | 1.90 | −1.53 | 1.54 | 5.97 | 0.09 | 126 | 6.03 | 0.07 | 13 | 4726 | 1.87 |
| 40 | 4700 | 1.70 | −1.48 | 1.60 | 6.01 | 0.10 | 132 | 6.09 | 0.06 | 13 | 4600 | 1.66 |
| 147 | 4860 | 2.07 | −1.49 | 1.40 | 6.01 | 0.09 | 125 | 6.08 | 0.08 | 13 | 4648 | 2.08 |
| 149 | 4920 | 2.15 | −1.47 | 1.46 | 6.03 | 0.10 | 122 | 6.11 | 0.07 | 13 | 4838 | 2.12 |
| 14 | 4880 | 2.15 | −1.48 | 1.54 | 6.02 | 0.09 | 129 | 6.09 | 0.06 | 13 | 4760 | 2.09 |
| 158 | 4910 | 2.20 | −1.56 | 1.42 | 5.94 | 0.11 | 117 | 6.00 | 0.06 | 12 | 4816 | 2.23 |
| 15 | 4880 | 2.20 | −1.42 | 1.48 | 6.08 | 0.09 | 125 | 6.16 | 0.04 | 13 | 4762 | 2.10 |
| 27 | 4880 | 2.10 | −1.39 | 1.48 | 6.11 | 0.09 | 122 | 6.18 | 0.07 | 13 | 4762 | 2.12 |
| 33 | 4950 | 2.35 | −1.58 | 1.37 | 5.92 | 0.10 | 110 | 5.97 | 0.07 | 13 | 4901 | 2.45 |
| 67 | 4990 | 2.36 | −1.68 | 1.41 | 5.82 | 0.10 | 111 | 5.88 | 0.09 | 13 | 4940 | 2.48 |
| 82 | 4860 | 2.05 | −1.44 | 1.49 | 6.06 | 0.08 | 128 | 6.14 | 0.09 | 13 | 4780 | 2.11 |
| 93 | 4950 | 2.33 | −1.46 | 1.55 | 6.03 | 0.09 | 124 | 6.11 | 0.06 | 13 | 4765 | 2.06 |
| 98 | 5000 | 2.53 | −1.55 | 1.36 | 5.95 | 0.09 | 112 | 6.01 | 0.08 | 13 | 4922 | 2.44 |

**Note.** The last two columns list the $T_{\rm eff}$ and log $g$ values obtained from photometry.

**Table 3**
Atomic Data and EWs for Program Stars

| Wavelength (Å) | Species | EP (eV) | log($gf$) | EW (mÅ) |
|---|---|---|---|---|
| | | 150 | | |
| 6806.860 | 26.0 | 2.730 | −3.140 | 21.9 |
| 4885.430 | 26.0 | 3.880 | −1.150 | 46.9 |
| 4917.240 | 26.0 | 4.190 | −1.270 | 32.5 |
| 6581.220 | 26.0 | 1.490 | −4.680 | 14.7 |
| 6592.910 | 26.0 | 2.730 | −1.490 | 99.2 |
| 6593.880 | 26.0 | 2.430 | −2.420 | 76.6 |
| 6608.040 | 26.0 | 2.280 | −3.960 | 10.8 |
| 6609.120 | 26.0 | 2.560 | −2.690 | 52.9 |
| 6627.560 | 26.0 | 4.550 | −1.500 | 6.6 |

(This table is available in its entirety in machine-readable form.)

rms of the average differences, i.e., about 50 K. The spectroscopic and photometric gravity scales agree, with an rms of 0.10 dex (bottom right panel). In the following, we adopt typical internal uncertainties of 50 K for $T_{\rm eff}$, 0.20 dex for log $g$, 0.20 km s$^{-1}$ for $\xi_t$, and 0.10 dex for metallicity but emphasize that systematic errors might be significantly larger. The adopted atmospheric parameters obtained from spectroscopy are listed in Table 2, where we also list the inferred Fe abundances and $T_{\rm eff}$/log $g$ values from photometry.

## 4. Chemical Abundance Analysis

In this work, we infer chemical abundances for 24 elements, namely Li, O, Na, Mg, Al, Si, Ca, Sc (II), Ti (I and II), V, Cr (I and II), Mn, Fe (I and II), Co, Ni, Cu, Zn, Y (II), Zr (II), Ba (II), La (II), Pr (II), Nd (II), and Eu (II). Chemical abundances were derived from an LTE analysis by using the MOOG code (Sneden 1973) and the $\alpha$-enhanced Kurucz model atmospheres of Castelli & Kurucz (2004), whose parameters have been obtained as described in Section 3. A list of our analyzed spectral lines, with their associated EWs, EPs, and total oscillator strengths (log $gf$), is provided in Table 3.

The chemical abundances for all elements, with the exception of those discussed below, have been inferred from an EW-based analysis. We now comment on some of the transitions that we used.

*Lithium.* Lithium abundances could be derived for 11 out of the 18 observed giants by spectral synthesis of the Li I $\lambda$6707 blend using the line list from Lind et al. (2009a) and Hobbs & Thorburn (1997). The abundances were then corrected for non-LTE effects following Lind et al. (2009a). The location on the CMD clearly suggests that the stars without detectable Li are brighter than the bump, suffering from strong Li depletions that occur at this luminosity. According to the red giant branch (RGB) bump $V$ mag provided by Nataf et al. (2013), two of the 11 stars with Li measurements are fainter than the bump; hence, their abundances might not be directly compared with those in pre-bump giants (see Table 4).

*Proton-capture elements.* In this group of elements, we have derived abundances for O, Na, Al, and Mg. Oxygen abundances were inferred from the synthesis of the forbidden [O I] line at 6300 Å. Telluric $O_2$ and $H_2O$ spectral absorptions often affect the O line at 6300 Å. Although telluric features have been removed, as detailed in Section 2.2 even with such a subtraction procedure, we caution that residual telluric feature contamination might be of concern for the analysis of the 6300.3 [O I] line. We determined Na abundances from the EWs of the Na I doublets at ∼5680 and ∼6150 Å, aluminum from the synthesis of the doublet at ∼6667 Å, and magnesium abundances from the EWs of the transitions at ∼5528, 5711 Å. Given the weakness of the Al doublet, for four stars, we could provide only an upper limit. Sodium abundances have been corrected for deviations from LTE (Lind et al. 2011).

*Manganese.* For Mn, we have synthesized the spectral lines at around 5395, 5420, 5433, 6014, and 6022 Å by assuming $f(^{55}\,{\rm Mn}) = 1.00$. When available, the hyperfine-splitting data have been taken from Lawler et al. (2001a, 2001b), otherwise from the Kurucz (2009) compendium.[11]

[11] http://kurucz.harvard.edu/

**Table 4**
Analyzed Chemical Abundances from Li to Sc

| Star | $A$(Li) LTE | $A$(Li) Non-LTE | [O/Fe] | $\sigma$ | No. | [Na/Fe] LTE | $\sigma$ | [Na/Fe] Non-LTE | No. | [Mg/Fe] | $\sigma$ | No. | [Al/Fe] | $\sigma$ | No. | [Si/Fe] | $\sigma$ | No. | [Ca/Fe] | $\sigma$ | No. | [Sc/Fe] | $\sigma$ | No. |
|---|---|---|---|---|---|---|---|---|---|---|---|---|---|---|---|---|---|---|---|---|---|---|---|---|
| 150 | <0.37[a] | ⋯ | 0.52 | 0.06 | 2 | −0.16 | 0.02 | −0.23 | 4 | 0.34 | 0.01 | 2 | −0.12 | 0.25 | 2 | 0.32 | 0.12 | 7 | 0.28 | 0.09 | 20 | −0.05 | 0.14 | 6 |
| 160 | <0.46[a] | ⋯ | 0.63 | ⋯ | 1 | −0.13 | 0.08 | −0.20 | 4 | 0.23 | 0.01 | 2 | −0.09 | ⋯ | 1 | 0.28 | 0.09 | 6 | 0.24 | 0.08 | 20 | 0.01 | 0.14 | 6 |
| 32 | 0.94[a] | 1.05 | 0.58 | 0.20 | 2 | −0.11 | 0.06 | −0.19 | 3 | 0.26 | 0.04 | 2 | −0.10 | ⋯ | 1 | 0.31 | 0.15 | 6 | 0.26 | 0.09 | 20 | 0.03 | 0.13 | 5 |
| 69 | 0.74[a] | 0.84 | 0.47 | ⋯ | 1 | −0.20 | 0.02 | −0.27 | 3 | 0.27 | 0.01 | 2 | <0.00 | ⋯ | ⋯ | 0.33 | 0.09 | 6 | 0.26 | 0.09 | 20 | 0.02 | 0.12 | 6 |
| 58 | <0.31[a] | ⋯ | 0.57 | 0.07 | 2 | −0.13 | 0.02 | −0.20 | 4 | 0.28 | 0.04 | 2 | −0.13 | 0.26 | 2 | 0.29 | 0.10 | 7 | 0.28 | 0.08 | 20 | −0.01 | 0.13 | 7 |
| 91 | <0.37[a] | ⋯ | 0.50 | ⋯ | 1 | −0.13 | 0.15 | −0.20 | 4 | 0.28 | 0.02 | 2 | −0.10 | 0.20 | 2 | 0.32 | 0.11 | 7 | 0.27 | 0.08 | 20 | 0.00 | 0.10 | 6 |
| 40 | <0.27[a] | ⋯ | 0.57 | 0.02 | 2 | −0.20 | 0.08 | −0.26 | 4 | 0.28 | 0.02 | 2 | −0.23 | ⋯ | 1 | 0.33 | 0.11 | 7 | 0.26 | 0.09 | 20 | 0.01 | 0.10 | 6 |
| 147 | 0.91 | 1.02 | 0.55 | ⋯ | 1 | −0.15 | 0.09 | −0.22 | 4 | 0.29 | 0.02 | 2 | <−0.10 | ⋯ | ⋯ | 0.26 | 0.09 | 7 | 0.27 | 0.10 | 20 | −0.07 | 0.13 | 6 |
| 149 | <0.50[a] | ⋯ | 0.50 | ⋯ | 1 | −0.06 | 0.13 | −0.14 | 4 | 0.27 | 0.02 | 2 | −0.18 | ⋯ | 1 | 0.32 | 0.11 | 7 | 0.26 | 0.08 | 20 | −0.02 | 0.14 | 6 |
| 14 | 0.94 | 1.04 | 0.54 | ⋯ | 1 | −0.18 | 0.04 | −0.26 | 4 | 0.27 | 0.03 | 2 | −0.13 | 0.20 | 2 | 0.30 | 0.10 | 5 | 0.26 | 0.09 | 20 | 0.00 | 0.14 | 6 |
| 158 | 0.95 | 1.04 | 0.60 | ⋯ | 1 | −0.15 | 0.16 | −0.22 | 4 | 0.25 | 0.02 | 2 | −0.13 | ⋯ | 1 | 0.33 | 0.12 | 5 | 0.26 | 0.09 | 20 | 0.01 | 0.12 | 5 |
| 15 | 0.93 | 1.03 | 0.59 | 0.09 | 2 | −0.16 | 0.06 | −0.24 | 4 | 0.26 | 0.02 | 2 | −0.05 | 0.30 | 2 | 0.32 | 0.09 | 5 | 0.28 | 0.08 | 20 | 0.04 | 0.12 | 5 |
| 27 | 0.97 | 1.07 | 0.48 | ⋯ | 1 | −0.28 | 0.07 | −0.35 | 4 | 0.20 | 0.01 | 2 | −0.26 | 0.19 | 2 | 0.28 | 0.09 | 6 | 0.24 | 0.09 | 19 | −0.03 | 0.09 | 6 |
| 33 | 0.80 | 0.88 | 0.63 | ⋯ | 1 | −0.18 | 0.04 | −0.26 | 2 | 0.24 | 0.01 | 2 | <0.10 | ⋯ | ⋯ | 0.30 | 0.10 | 6 | 0.28 | 0.07 | 18 | −0.03 | 0.14 | 6 |
| 67 | 0.87 | 0.94 | 0.59 | ⋯ | 1 | −0.19 | 0.21 | −0.25 | 4 | 0.27 | 0.01 | 2 | <−0.10 | ⋯ | ⋯ | 0.29 | 0.10 | 6 | 0.24 | 0.08 | 19 | −0.02 | 0.20 | 6 |
| 82 | 0.80 | 0.91 | 0.58 | 0.02 | 2 | −0.17 | 0.10 | −0.25 | 4 | 0.22 | 0.01 | 2 | −0.13 | 0.08 | 2 | 0.28 | 0.09 | 7 | 0.25 | 0.09 | 20 | −0.03 | 0.14 | 6 |
| 93 | <0.44[a] | ⋯ | 0.71 | 0.02 | 2 | −0.16 | 0.12 | −0.24 | 4 | 0.28 | 0.00 | 2 | −0.33 | ⋯ | 1 | 0.35 | 0.10 | 5 | 0.23 | 0.09 | 20 | 0.05 | 0.10 | 5 |
| 98 | 0.90 | 0.97 | 0.68 | ⋯ | 1 | −0.22 | 0.22 | −0.29 | 4 | 0.22 | 0.00 | 2 | −0.10 | 0.38 | 2 | 0.28 | 0.08 | 7 | 0.25 | 0.08 | 19 | −0.04 | 0.09 | 6 |
| Avg. | 0.89 | 0.98 | 0.57 | | | −0.16 | | −0.23 | | 0.26 | | | −0.15 | | | 0.31 | | | 0.26 | | | −0.01 | | |
| ± | 0.02 | 0.02 | 0.02 | | | 0.01 | | 0.01 | | 0.01 | | | 0.02 | | | 0.01 | | | 0.00 | | | 0.01 | | |
| $\sigma$ | 0.07 | 0.08 | 0.07 | | | 0.05 | | 0.05 | | 0.03 | | | 0.08 | | | 0.02 | | | 0.02 | | | 0.03 | | |

**Note.**
[a] Star brighter than the RGB bump.

*Copper.* Abundances for Cu were inferred from synthesis of the Cu I line at around 5105 Å. Both hyperfine and isotopic splitting were included in the analysis using the well-studied spectral line component structure from Kurucz (2009). Solar system isotopic fractions were assumed in the computations: $f(^{63}\mathrm{Cu}) = 0.69$ and $f(^{65}\mathrm{Cu}) = 0.31$.

*Neutron-capture elements.* In the group of neutron-capture (*n*-capture) elements, we derived abundances for Y, Zr, Ba, La, Pr, Nd, and Eu. For most of these elements, we performed a spectral synthesis analysis, as hyperfine and/or isotopic splitting and/or blending features needed to be taken into account.

Specifically, spectral synthesis was employed for Zr (5112 Å), Ba (5854, 6142, and 6497 Å), La (4921, 5115, 5291, 5304, 6262, 6390, and 6774 Å), Pr (5323 Å), and Eu (6645 Å). Our Ba abundances were computed assuming the McWilliam (1998) *r*-process isotopic composition and hyperfine splitting. In all other cases, we have assumed the solar system isotopic fractions.

The inferred chemical abundances are listed in Tables 4–6. Internal uncertainties to these abundances due to the adopted model atmospheres were estimated by varying the stellar parameters, one at a time, by the amounts estimated in Section 3, namely $T_{\rm eff}/\log g/[\mathrm{A/H}]/\xi_{\rm t} = \pm 50\,\mathrm{K}/\pm 0.20\,\mathrm{cgs}/\pm 0.10\,\mathrm{dex}/\pm 0.20\,\mathrm{km\,s^{-1}}$. In addition to the contribution introduced by internal errors in atmospheric parameters, we estimated the contribution due to the limits of our spectra, e.g., due to the finite S/N that affects the measurements of EWs and the spectral synthesis.

To estimate the contribution to the internal uncertainties given by the quality of the spectra ($\sigma_{\rm EWs/fit}$), we have compared the EWs obtained from individual exposures of the same stars. For this comparison, we use a relatively bright star (58) with five exposures and a fainter star (158) with one exposure. We get a typical error in EW of ∼1.5 mÅ, obtained as the average rms of the EW measurements for each line divided by $\sqrt{(N-1)}$, where $N$ is the number of exposures. For each element, the errors in chemical abundances due to the EWs have been calculated by varying the EWs of the spectral lines by the corresponding uncertainty. For the species inferred from spectral synthesis, we have varied the continuum at the $\pm 1\sigma$ level and rederived the chemical abundances from each line.

For the spectral lines analyzed with synthesis, we follow the approach by Norris et al. (2010) and Yong et al. (2013b). For each element, we replace the rms ($\sigma$) in Tables 4–6 with the maximum $\sigma$ value. Then, we derive $\max(\sigma)/\sqrt{N_{\rm lines}}$. For those elements whose abundance is inferred from just one line, we use the typical uncertainty introduced by the continuum scatter as our $\sigma_{\rm EWs/fit}$. The typical values obtained for each element are listed in column 8 of Table 7. The total error is obtained by quadratically adding this random error with the uncertainties introduced by atmospheric parameters.

Since the EWs/continuum placement errors are random, the uncertainty associated with those elements with a larger number of lines is lower. Hence, the corresponding uncertainty associated with Fe I is negligible, while for those species inferred from one or two weak spectral lines, the error due to the limited S/N is dominant (e.g., O, Al, Zr, Pr, and Eu).

## 5. The Chemical Composition along the First Population of NGC 3201

In this section, we explore the chemical composition in different elemental species along the elongated 1G observed on the ChM of NGC 3201. We emphasize that, although the range covered by our targets in the $\Delta_{\rm F275W,F814W}$ axis is large, they span only a small range in $\Delta_{C\ \rm F275W,F336W,F438W}$, and their position on the map is consistent with the 1G, as defined by Milone et al. (2015, 2017). As the $\Delta_{C\ \rm F275W,F336W,F438W}$ axis of the ChM is shaped by light-element variations primarily driven by the N enhancements in the 2G stars, we expect homogeneous abundances in this chemical species (Marino et al. 2019).

Overall, for our 18 giants, we obtain a mean iron abundance of $[\mathrm{Fe/H}] = -1.50 \pm 0.02$ dex (rms = 0.07 dex), consistent with the value of $[\mathrm{Fe/H}] = -1.59$ listed in Harris (2010). Figure 3 shows a summary of the other chemical abundance ratios obtained for our 1G sample of NGC 3201 stars.[12] Besides observing the typical chemical pattern of Population II stars, namely the enhancement in the $\alpha$-elements (Mg, Si, Ca, Ti), and the typical solar-scaled abundances of Fe-peak elements, more interesting for this study is the investigation of the elements that have a close connection with the shape of the ChM.

In Figure 3, we show a comparison of our results for NGC 3201 with all of the GCs for which abundances on ChMs are available from Marino et al. (2019; Table 2). Overall, our inferred abundances agree with those observed in the 1G as selected on the ChM of GCs, as expected from the location of our targets along the ChM of NGC 3201. In the next sections, we will discuss all of the interesting abundance patterns we observe in NGC 3201, focusing on those elements that play an important role in the multiple stellar population phenomenon and shaping the ChM. In particular, Marino et al. (2019) analyzed the chemical abundance pattern along the ChM for the species most involved in the multiple stellar population phenomenon, namely the *p*-capture (e.g., O, Na, Mg, Al) and *n*-capture (Ba) elements.

First, we note that the abundances relative to Fe ([X/Fe]) are generally consistent with uniform chemical abundances in the plotted elements. By comparing the observed rms associated with the mean average abundances, as listed in Tables 4–6, with the estimated errors (Table 7), it appears that, in most cases, our expected uncertainties are higher. This suggests that our estimated errors might be overestimated. Exceptions to this general trend are the *n*-capture elements, which will be discussed in the following sections.

As already mentioned, the chemical abundances of the 18 stars of NGC 3201 analyzed here are consistent with the chemical composition of 1G stars. Lithium abundances have a range of ∼0.2 dex, from $A(\mathrm{Li}) \sim 0.75$ to 1.0 dex, which compares to typical values of RGB stars that have experienced the full first dredge up but not yet reached the RGB bump level (Lind et al. 2009b). As highlighted in Table 4, stars with only upper limits plus two other stars with Li measurements are brighter than the RGB bump. In the context of multiple stellar populations, Marino et al. (2019) did not find strong evidence for variations of Li between 1G and 2G stars on the ChM, with the exception of GCs like NGC 2808 and $\omega$ Centauri. Hence, the comparison of Li with the average abundances of 1G and 2G stars in all of the GCs, as shown in Figure 3, does not likely

[12] Chemical abundances are expressed in the standard notation as the logarithmic ratios with respect to solar values, $[\mathrm{X/Y}] = \log\left(\frac{N_{\rm X}}{N_{\rm Y}}\right)_{\rm star} - \log\left(\frac{N_{\rm X}}{N_{\rm Y}}\right)_{\odot}$. For lithium, abundances are reported as $A(\mathrm{Li}) = \log\left(\frac{N_{\rm Li}}{N_{\rm H}}\right)_{\rm star} + 12$.

**Table 5**
Analyzed Chemical Abundances from Ti to Ni

| Star | [Ti/Fe]I | $\sigma$ | No. | [Ti/Fe]II | $\sigma$ | No. | [V/Fe] | $\sigma$ | No. | [Cr/Fe]I | $\sigma$ | No. | [Cr/Fe]II | $\sigma$ | No. | [Mn/Fe] | $\sigma$ | No. | [Co/Fe] | $\sigma$ | No. | [Ni/Fe] | $\sigma$ | No. |
|---|---|---|---|---|---|---|---|---|---|---|---|---|---|---|---|---|---|---|---|---|---|---|---|---|
| 150 | 0.19 | 0.09 | 20 | 0.24 | 0.05 | 5 | −0.10 | 0.09 | 14 | −0.08 | 0.09 | 4 | 0.10 | 0.02 | 2 | −0.50 | 0.10 | 5 | −0.12 | 0.07 | 2 | −0.06 | 0.11 | 23 |
| 160 | 0.25 | 0.12 | 20 | 0.21 | 0.09 | 5 | −0.06 | 0.11 | 13 | −0.08 | 0.11 | 4 | 0.10 | 0.03 | 2 | −0.46 | 0.07 | 5 | −0.23 | 0.00 | 2 | −0.03 | 0.12 | 23 |
| 32 | 0.19 | 0.11 | 20 | 0.25 | 0.03 | 5 | −0.09 | 0.09 | 14 | −0.09 | 0.10 | 4 | 0.05 | 0.02 | 2 | −0.45 | 0.09 | 5 | −0.17 | 0.18 | 2 | −0.04 | 0.14 | 24 |
| 69 | 0.25 | 0.12 | 18 | 0.29 | 0.05 | 5 | −0.02 | 0.11 | 9 | −0.15 | 0.07 | 4 | 0.16 | 0.02 | 2 | −0.49 | 0.08 | 5 | −0.09 | 0.01 | 2 | −0.04 | 0.13 | 20 |
| 58 | 0.24 | 0.09 | 22 | 0.26 | 0.04 | 5 | −0.03 | 0.08 | 14 | −0.06 | 0.08 | 4 | 0.15 | 0.02 | 2 | −0.40 | 0.05 | 5 | −0.16 | 0.15 | 2 | 0.01 | 0.12 | 25 |
| 91 | 0.19 | 0.12 | 20 | 0.24 | 0.06 | 5 | −0.11 | 0.12 | 13 | −0.15 | 0.12 | 4 | 0.07 | 0.02 | 2 | −0.50 | 0.12 | 5 | −0.10 | 0.15 | 2 | −0.04 | 0.11 | 22 |
| 40 | 0.20 | 0.08 | 21 | 0.26 | 0.07 | 5 | −0.06 | 0.08 | 14 | −0.10 | 0.08 | 4 | 0.10 | 0.06 | 2 | −0.46 | 0.06 | 5 | −0.07 | 0.00 | 2 | −0.02 | 0.14 | 24 |
| 147 | 0.24 | 0.09 | 19 | 0.27 | 0.05 | 5 | −0.10 | 0.07 | 13 | −0.08 | 0.10 | 4 | 0.10 | 0.12 | 2 | −0.48 | 0.12 | 5 | −0.23 | 0.09 | 2 | −0.05 | 0.12 | 21 |
| 149 | 0.17 | 0.08 | 19 | 0.17 | 0.03 | 5 | −0.07 | 0.11 | 11 | −0.13 | 0.08 | 4 | 0.05 | 0.01 | 2 | −0.55 | 0.12 | 5 | −0.15 | ⋯ | 1 | −0.07 | 0.10 | 21 |
| 14 | 0.23 | 0.07 | 22 | 0.27 | 0.08 | 5 | −0.02 | 0.06 | 9 | −0.05 | 0.11 | 4 | 0.18 | 0.02 | 2 | −0.44 | 0.06 | 5 | −0.20 | ⋯ | 1 | −0.01 | 0.10 | 24 |
| 158 | 0.21 | 0.11 | 17 | 0.21 | 0.03 | 5 | −0.09 | 0.10 | 7 | −0.21 | 0.10 | 3 | 0.10 | 0.05 | 2 | −0.58 | 0.12 | 5 | ⋯ | ⋯ | ⋯ | −0.04 | 0.12 | 20 |
| 15 | 0.20 | 0.06 | 21 | 0.25 | 0.05 | 5 | −0.02 | 0.09 | 11 | −0.11 | 0.06 | 4 | 0.11 | 0.04 | 2 | −0.50 | 0.10 | 5 | −0.10 | 0.05 | 2 | −0.02 | 0.12 | 24 |
| 27 | 0.15 | 0.08 | 21 | 0.19 | 0.05 | 5 | −0.04 | 0.09 | 10 | −0.11 | 0.06 | 4 | −0.01 | 0.14 | 2 | −0.50 | 0.08 | 5 | −0.14 | 0.03 | 2 | −0.04 | 0.11 | 24 |
| 33 | 0.16 | 0.06 | 15 | 0.25 | 0.05 | 5 | −0.04 | 0.14 | 4 | −0.19 | 0.07 | 3 | 0.05 | 0.10 | 2 | −0.54 | 0.13 | 5 | 0.04 | ⋯ | 1 | −0.07 | 0.14 | 17 |
| 67 | 0.21 | 0.07 | 14 | 0.18 | 0.11 | 5 | −0.07 | 0.08 | 6 | −0.25 | 0.12 | 2 | 0.17 | 0.08 | 2 | −0.50 | 0.14 | 5 | ⋯ | ⋯ | ⋯ | −0.08 | 0.12 | 15 |
| 82 | 0.22 | 0.08 | 20 | 0.24 | 0.08 | 5 | −0.08 | 0.12 | 13 | −0.09 | 0.07 | 4 | 0.07 | 0.01 | 2 | −0.47 | 0.08 | 5 | −0.20 | 0.07 | 2 | −0.02 | 0.10 | 24 |
| 93 | 0.24 | 0.09 | 19 | 0.32 | 0.07 | 5 | −0.05 | 0.07 | 9 | −0.05 | 0.15 | 4 | 0.17 | 0.02 | 2 | −0.47 | 0.10 | 5 | −0.19 | 0.19 | 2 | −0.03 | 0.10 | 22 |
| 98 | 0.17 | 0.08 | 18 | 0.22 | 0.06 | 5 | −0.06 | 0.17 | 6 | −0.15 | 0.10 | 4 | 0.07 | 0.08 | 2 | −0.49 | 0.15 | 5 | ⋯ | ⋯ | ⋯ | −0.07 | 0.10 | 18 |
| Avg. | 0.21 | | | 0.24 | | | −0.06 | | | −0.12 | | | 0.10 | | | −0.49 | | | −0.14 | | | −0.04 | | |
| ± | 0.01 | | | 0.01 | | | 0.01 | | | 0.01 | | | 0.01 | | | 0.01 | | | 0.02 | | | 0.01 | | |
| $\sigma$ | 0.03 | | | 0.04 | | | 0.03 | | | 0.06 | | | 0.05 | | | 0.04 | | | 0.07 | | | 0.02 | | |

**Table 6**
Analyzed Chemical Abundances from Cu to Eu

| Star | [Cu/Fe] | [Zn/Fe] | [Y/Fe] | $\sigma$ | No. | [Zr/Fe] | [Ba/Fe] | $\sigma$ | No. | [La/Fe] | $\sigma$ | No. | [Pr/Fe] | [Nd/Fe] | $\sigma$ | No. | [Eu/Fe] |
|---|---|---|---|---|---|---|---|---|---|---|---|---|---|---|---|---|---|
| 150 | −0.57 | 0.13 | −0.24 | 0.07 | 3 | 0.04 | 0.20 | 0.04 | 3 | 0.17 | 0.09 | 7 | 0.23 | 0.10 | 0.03 | 2 | 0.45 |
| 160 | −0.55 | 0.19 | −0.18 | 0.08 | 3 | 0.11 | 0.33 | 0.05 | 3 | 0.27 | 0.11 | 5 | 0.33 | 0.25 | 0.02 | 2 | 0.60 |
| 32 | −0.57 | 0.18 | −0.21 | 0.07 | 2 | 0.03 | 0.32 | 0.03 | 3 | 0.25 | 0.07 | 6 | 0.32 | 0.28 | 0.06 | 2 | 0.56 |
| 69 | −0.65 | 0.14 | −0.20 | 0.12 | 2 | 0.04 | 0.21 | 0.04 | 3 | 0.25 | 0.05 | 6 | 0.33 | 0.20 | 0.05 | 2 | 0.47 |
| 58 | −0.34 | 0.23 | −0.24 | 0.07 | 3 | 0.16 | 0.25 | 0.02 | 3 | 0.24 | 0.08 | 7 | 0.30 | 0.27 | 0.08 | 2 | 0.56 |
| 91 | −0.57 | 0.07 | −0.17 | 0.15 | 3 | 0.02 | 0.21 | 0.01 | 3 | 0.14 | 0.05 | 6 | 0.32 | 0.13 | 0.04 | 2 | 0.28 |
| 40 | −0.50 | 0.13 | −0.27 | 0.04 | 3 | 0.13 | 0.19 | 0.06 | 3 | 0.18 | 0.06 | 6 | 0.18 | 0.13 | 0.07 | 2 | 0.43 |
| 147 | −0.55 | 0.20 | −0.27 | 0.03 | 3 | −0.01 | 0.27 | 0.05 | 3 | 0.27 | 0.06 | 6 | 0.40 | 0.17 | 0.09 | 2 | 0.54 |
| 149 | −0.64 | 0.01 | −0.19 | 0.04 | 3 | 0.15 | 0.68 | 0.04 | 3 | 0.47 | 0.07 | 6 | 0.45 | 0.42 | 0.01 | 2 | 0.45 |
| 14 | −0.52 | 0.14 | −0.15 | 0.17 | 3 | 0.02 | 0.30 | 0.07 | 3 | 0.29 | 0.06 | 6 | 0.20 | 0.19 | 0.05 | 2 | 0.55 |
| 158 | −0.70 | −0.03 | −0.26 | 0.01 | 2 | 0.09 | 0.22 | 0.08 | 3 | 0.20 | 0.13 | 2 | <0.55 | 0.09 | 0.00 | 2 | <0.70 |
| 15 | −0.61 | 0.11 | −0.19 | 0.10 | 3 | 0.20 | 0.29 | 0.07 | 3 | 0.28 | 0.09 | 4 | 0.34 | 0.17 | 0.00 | 2 | 0.50 |
| 27 | −0.62 | 0.04 | −0.32 | 0.12 | 3 | 0.01 | 0.19 | 0.04 | 3 | 0.17 | 0.12 | 6 | 0.35 | 0.08 | 0.04 | 2 | 0.45 |
| 33 | −0.67 | 0.21 | −0.23 | 0.10 | 2 | 0.22 | 0.23 | 0.04 | 3 | 0.19 | 0.01 | 2 | <0.70 | 0.21 | 0.00 | 2 | 0.41 |
| 67 | −0.75 | −0.01 | −0.33 | 0.06 | 2 | −0.05 | 0.15 | 0.10 | 3 | 0.19 | 0.03 | 2 | <0.80 | 0.10 | 0.01 | 2 | 0.45 |
| 82 | −0.52 | 0.12 | −0.21 | 0.07 | 3 | 0.08 | 0.30 | 0.10 | 3 | 0.26 | 0.08 | 7 | 0.30 | 0.19 | 0.07 | 2 | 0.48 |
| 93 | −0.59 | 0.12 | 0.11 | 0.07 | 3 | 0.33 | 1.16 | 0.04 | 3 | 0.90 | 0.07 | 7 | 0.80 | 0.91 | 0.03 | 2 | 0.65 |
| 98 | −0.60 | 0.03 | −0.30 | 0.07 | 2 | ⋯ | 0.23 | 0.08 | 3 | 0.26 | 0.14 | 2 | <0.50 | 0.10 | 0.01 | 2 | 0.35 |
| Avg. | −0.58 | 0.11 | −0.21 | | | 0.09 | 0.32 | | | 0.28 | | | 0.35 | 0.22 | | | 0.48 |
| ± | 0.02 | 0.02 | 0.02 | | | 0.02 | 0.06 | | | 0.04 | | | 0.04 | 0.05 | | | 0.02 |
| $\sigma$ | 0.09 | 0.08 | 0.10 | | | 0.10 | 0.24 | | | 0.17 | | | 0.15 | 0.19 | | | 0.09 |

**Table 7**
Sensitivity of the Derived Abundances to the Uncertainties in Atmospheric Parameters ($T_{\rm eff}$/log $g$/$\xi_{\rm t}$/[A/H] = ±50 K/±0.20/±0.20 km s$^{-1}$/±0.10) and Due to the Errors in the EW Measurements or $\chi^2$ Fitting Procedure

| (1) | $\Delta T_{\rm eff}$ ±100 K (2) | $\Delta T_{\rm eff}$ ±50 K (3) | $\Delta$log $g$ ±0.20 (4) | $\Delta\xi_{\rm t}$ ±0.20 km s$^{-1}$ (5) | $\Delta$[A/H] ±0.10 dex (6) | $\sigma_{\rm EWs/fit}$ (7) | $\sigma_{\rm total}$ (8) |
|---|---|---|---|---|---|---|---|
| $A$(Li) | ±0.15 | ±0.10 | ±0.02 | ±0.03 | ±0.00 | ±0.10 | ±0.15 |
| [O/Fe] | ±0.03 | ±0.20 | ±0.08 | ±0.00 | ±0.03 | ±0.01 | ±0.22 |
| [Na/Fe] | ∓0.06 | ±0.05 | ∓0.02 | ±0.04 | ∓0.01 | ∓0.02 | ±0.07 |
| [Mg/Fe] | ∓0.06 | ±0.02 | ∓0.04 | ∓0.03 | ∓0.02 | ∓0.02 | ±0.08 |
| [Al/Fe] | ±0.05 | ±0.27 | ∓0.01 | ±0.00 | ∓0.01 | ±0.02 | ±0.27 |
| [Si/Fe] | ∓0.08 | ±0.02 | ±0.03 | ±0.05 | ±0.03 | ∓0.05 | ±0.08 |
| [Ca/Fe] | ∓0.03 | ±0.01 | ∓0.01 | ∓0.01 | ±0.00 | ∓0.01 | ±0.02 |
| [Sc/Fe] II | ±0.09 | ±0.02 | ±0.04 | ±0.07 | ±0.05 | ±0.03 | ±0.10 |
| [Ti/Fe] I | ±0.03 | ±0.01 | ∓0.01 | ±0.03 | ±0.00 | ±0.02 | ±0.04 |
| [Ti/Fe] II | ±0.08 | ±0.02 | ±0.04 | ±0.05 | ±0.05 | ±0.02 | ±0.09 |
| [V/Fe] | ±0.07 | ±0.03 | ±0.02 | ±0.07 | ±0.03 | ±0.02 | ±0.09 |
| [Cr/Fe] I | ∓0.03 | ±0.03 | ∓0.06 | ∓0.04 | ∓0.05 | ∓0.01 | ±0.092 |
| [Cr/Fe] II | ±0.02 | ±0.05 | ±0.01 | ±0.04 | ±0.01 | ±0.00 | ±0.07 |
| [Mn/Fe] | ±0.03 | ±0.07 | ∓0.02 | ±0.04 | ∓0.01 | ±0.01 | ±0.08 |
| [Fe/H] I | ±0.13 | ±0.00 | ±0.01 | ∓0.04 | ±0.01 | ±0.06 | ±0.07 |
| [Fe/H] II | ∓0.07 | ±0.01 | ±0.08 | ∓0.07 | ±0.01 | ∓0.02 | ±0.11 |
| [Co/Fe] | ±0.04 | ±0.06 | ±0.04 | ±0.09 | ±0.05 | ±0.00 | ±0.13 |
| [Ni/Fe] | ∓0.01 | ±0.01 | ±0.01 | ±0.04 | ±0.01 | ∓0.01 | ±0.04 |
| [Cu/Fe] | ±0.14 | ±0.10 | ∓0.00 | ∓0.03 | ∓0.01 | ±0.07 | ±0.13 |
| [Zn/Fe] | ∓0.14 | ±0.05 | ±0.05 | ∓0.04 | ±0.01 | ∓0.07 | ±0.11 |
| [Y/Fe] II | ±0.07 | ±0.05 | ∓0.01 | ±0.01 | ±0.01 | ±0.03 | ±0.06 |
| [Zr/Fe] II | ∓0.04 | ±0.15 | ±0.10 | ∓0.00 | ±0.05 | ∓0.02 | ±0.19 |
| [Ba/Fe] II | ±0.03 | ±0.10 | ±0.07 | ∓0.15 | ±0.03 | ±0.01 | ±0.20 |
| [La/Fe] II | ±0.03 | ±0.07 | ±0.07 | ∓0.01 | ±0.03 | ±0.01 | ±0.10 |
| [Pr/Fe] II | ±0.04 | ±0.15 | ±0.07 | ±0.00 | ±0.05 | ±0.01 | ±0.17 |
| [Nd/Fe] II | ±0.14 | ±0.06 | ±0.06 | ±0.09 | ±0.07 | ±0.05 | ±0.15 |
| [Eu/Fe] II | ±0.00 | ±0.15 | ±0.08 | ±0.00 | ±0.04 | ∓0.00 | ±0.17 |

**Note.** For reference, we also list the variations due to a change in $T_{\rm eff}$ by ±100 K. We reported the total internal uncertainty ($\sigma_{\rm total}$) obtained by the quadratic sum of all of the contributors to the error.

provide clear information on the population status of our sample in NGC 3201.

Oxygen and sodium are the best tracers of the multiple stellar population phenomenon, and their abundances are indicative of different locations along the ChM. Specifically, for our NGC 3201 giants, the oxygen abundances relative to iron are supersolar, as is typical of Population II stars, while sodium is not enhanced. Both of these elements show distributions compatible with the 1G ones. The association of all of the analyzed stars with the chemical composition of the ChM 1G is clear by looking at their location on the $\delta_{\rm [O/Fe]}$–$\delta_{\rm [Na/Fe]}$ plane plotted in Figure 4, where the $\delta$ abundances are the relative abundances to the average chemical content of 1G stars in each cluster (see Marino et al. 2019, for a detailed discussion).

Chemical enhancements in aluminum coupled with depletions in magnesium are observed in a few clusters, with NGC 2808 being a noticeable example. Both our Mg and Al abundances fall in the range spanned by 1G stars. Magnesium relative to Fe is supersolar, as expected from a typical $\alpha$-element, and the Al abundances distribute on the lower abundance tail spanned by 1G stars. Neither of these element distributions show any evidence for internal variations within our 18 analyzed stars. The location of our stars on the $\delta_{\rm [Mg/Fe]}$–$\delta_{\rm [Al/Fe]}$ plane, constructed by using relative abundances similar to those used for $\delta_{\rm [O/Fe]}$ and $\delta_{\rm [Na/Fe]}$, are plotted in the right panel of Figure 4.

## 6. Binarity and BSs

Noticeably, Figure 3 shows a few stars with significantly higher abundances in the *n*-capture elements, Y, Ba, La, Pr, and Nd. This class of chemical species plays an important role in the Type II GCs, those displaying additional ChMs on the red side of the main map. Stars on the red side of the ChMs are typically enhanced in both Fe and the elements mostly produced via *s*-process reactions, e.g., Ba and La, but not in Eu, a typical *r*-process element. Nevertheless, NGC 3201 does not belong to the class of Type II GCs, as it does not show a clear additional redder sequence in the ChM, as M22, M2, or $\omega$ Centauri do (Milone et al. 2017).

To investigate the nature of the variations in *s*-process elements in NGC 3201, we plot in Figure 5 the abundance of [La/Fe] taken as representative of the *s*-process elements as a function of the rms in the RVs (left panel) and $\Delta_{\rm F275W,F814W}$ (right panel). While most stars show typical [La/Fe] abundances around 0.25 dex, two stars have [La/Fe] $>$ 0.40 dex, with one reaching an abundance as high as [La/Fe] = 0.90 dex. Interestingly, this extremely La-rich star (star 93) also has a high rms in RV ($\sigma_{\rm RV}$), compared to the bulk of the stars lying around 0.2 km s$^{-1}$. A third outlier in the [La/Fe]–$\sigma_{\rm RV}$ plane displays the highest rms in RV (0.76 km s$^{-1}$, star 67), but it is not an outlier for [La/Fe].

The high RV rms in two giants of our sample suggests that these stars are indeed binaries. By applying a maximum

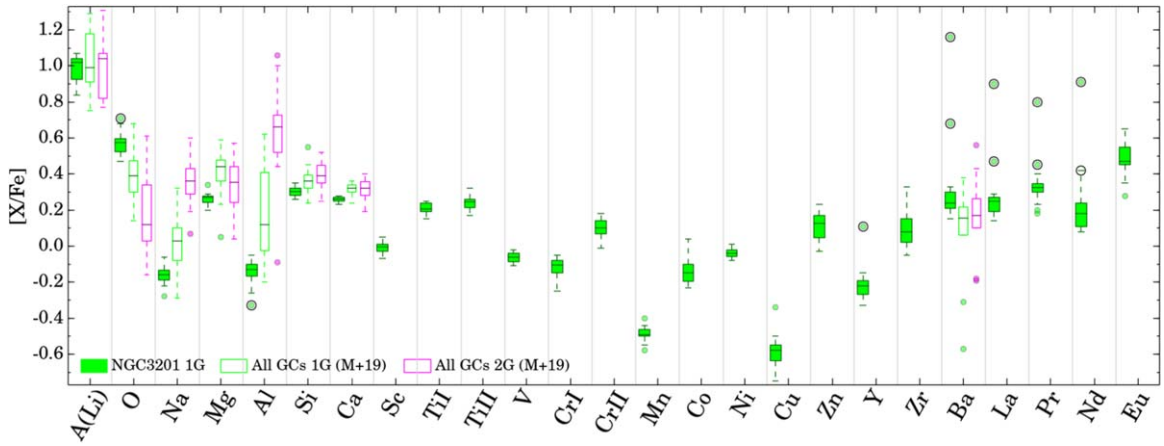


**Figure 3.** Box-and-whisker plot for the chemical abundances of the 1G stars observed on the ChM of NGC 3201 (green filled boxes). All of the abundances are relative to Fe, except for Li, for which we use the usual $A$(Li) notation. Plotted Li abundances are corrected for non-LTE effects. As a comparison, we also show the box-and-whisker plots for all of the GCs for which abundances on ChMs are available. These boxes have been constructed with the average abundances for 1G and 2G listed in Table 2 from Marino et al. (2019). The 1G and 2G average abundances for all GCs are represented with green and magenta open boxes. Each box represents the interquartile range (IQR) of the distribution, with the median abundance marked by a horizontal line. The whiskers include observations that fall below the first quartile minus 1.5 × IQR or above the third quartile plus 1.5 × IQR. As the majority of the used literature studies for Na report LTE abundances, the plotted [Na/Fe] values for NGC 3201 are not corrected for non-LTE. Small filled circles represent outliers in the data. Outliers highlighted with black open circles are the candidate binaries (see Section 6 for details).

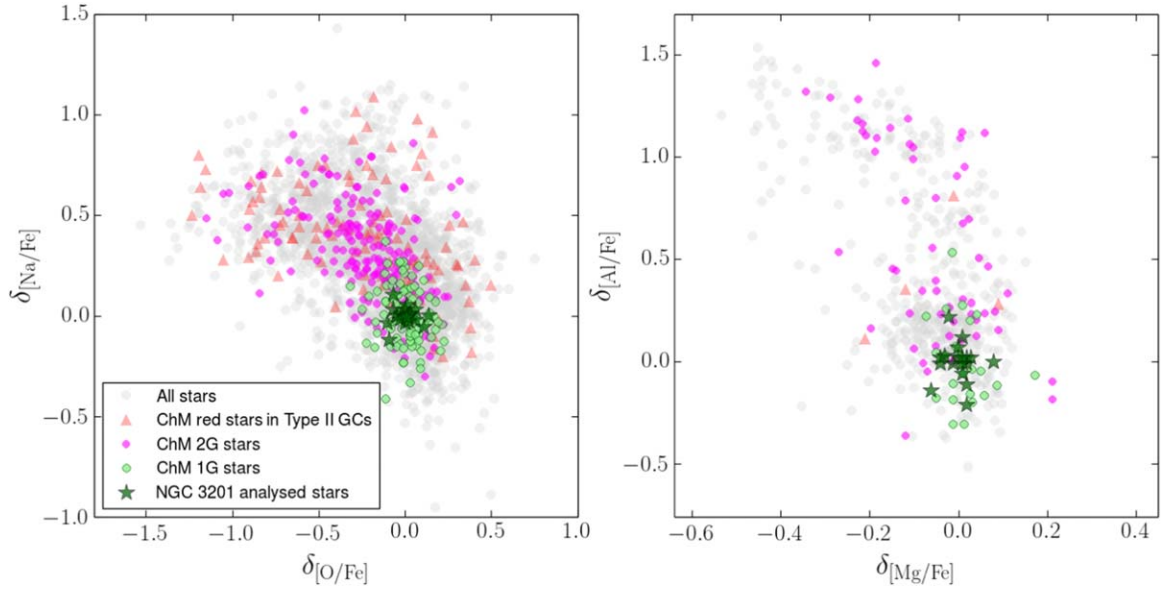


**Figure 4.** Abundance ratios of $\delta_{[Na/Fe]}$ as a function of $\delta_{[O/Fe]}$ (left) and $\delta_{[Al/Fe]}$ as a function of $\delta_{[Mg/Fe]}$ (right) for all GCs analyzed in Marino et al. (2019). The plotted abundances are relative to the average abundances of 1G stars, as defined by Marino and collaborators. Different symbols and colors represent stars belonging to different populations on the ChM. The abundances of the analyzed stars in NGC 3201 perfectly overlap with the ChM 1G abundances on these $\delta_{[O/Fe]}$–$\delta_{[Na/Fe]}$ and $\delta_{[Mg/Fe]}$–$\delta_{[Al/Fe]}$ planes.

likelihood approach similar to that used in Frank et al. (2015) and Piatti & Koch (2018), assuming a typical uncertainty of 0.17 km s$^{-1}$, we found that the intrinsic dispersions in the RVs of stars 93 and 67 are 0.51 and 0.74 km s$^{-1}$, respectively. Such values, higher than zero, corroborate the idea that these stars are binary candidates. The very high abundance in *s*-elements of one of these stars is consistent with the binary nature of this object. Similarly, star 149 having relatively high abundances in *s*-elements can be regarded as a binary candidate, although our data do not show any evidence of high variations in its RV.

As shown in Figure 6, the stars with high *n*-capture element abundances also show higher [hs/ls] than the mean value of ∼0.5 dex, suggesting that they are likely the result of direct mass transfer with a low-mass asymptotic giant branch (AGB) companion. The abundance ratios [La/Y] and [Ba/Y] as a function of $\Delta_{F275W,F814W}$ are indicative of the heavy-to-light *n*-capture element abundance ratio, which is sensitive to the neutron exposure and density. Higher [hs/ls] is indicative of the operation of the $^{13}C(\alpha,n)^{16}O$ neutron source operating in low-mass AGB stars (e.g., Gallino et al. 1998; Fishlock et al. 2014), where values around zero or negative values indicate the $^{22}Ne(\alpha,n)^{25}Mg$ reaction. The higher [hs/ls] of the two giants enriched in *n*-capture elements might suggest direct mass transfer between the star we now observe and previous low-mass, low-metallicity AGB stars (e.g., Cristallo et al. 2009; Karakas & Lattanzio 2014).

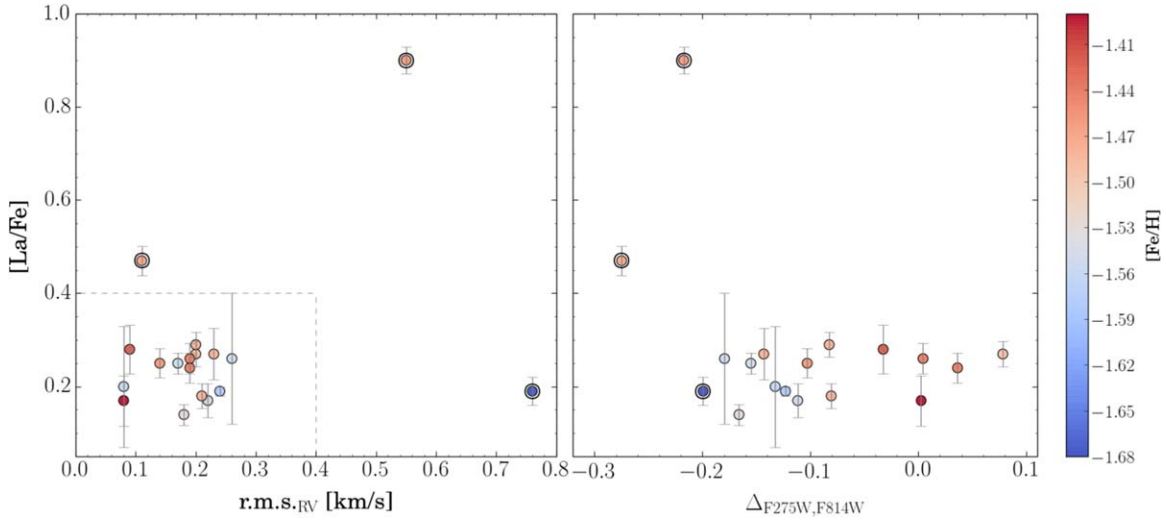


**Figure 5.** Abundance of the *n*-capture element La relative to Fe as a function of the rms in the RVs (left panel) and $\Delta_{F275W,F814W}$ (right panel). Error bars are the statistical errors associated with the average abundances for each star obtained from different lines. The color of each star is indicative of its inferred Fe, as illustrated in the color bar. Our three binary candidates, outlined with black circles, lie outside the box delimited by a dashed line in the left panel.

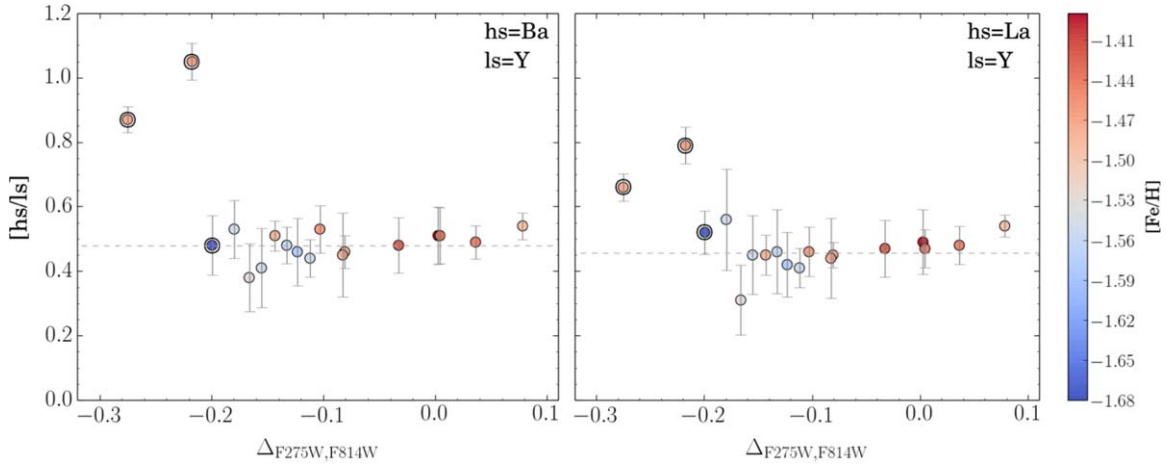


**Figure 6.** Abundance of [Ba/Y] (left) and [La/Y] (right), representative of the heavy-to-light *s*-element abundances ([hs/ls]), as a function of $\Delta_{F275W,F814W}$. The dashed lines in both panels highlight the average abundance ratios for the entire sample, neglecting the three (encircled) binary candidates. As in Figure 5, the color of each star is indicative of its inferred Fe, as illustrated in the color bar.

In the last column of Table 1, we list the maximum time interval between the observations of each star. We note that some stars, including star 149, have been observed over a shorter time interval (3 days rather than months), which might have prevented us from detecting RV measurable variations in longer-period binaries.

In the following, we will consider these three stars as binary candidates. Their locations in Figures 2, 3 and 5 (as well as in some of the following figures) are highlighted with black open circles. We warn the reader that we cannot rule out the presence of other binaries with no obvious *s*-elements and/or RV differences among our remaining 15 giants.

Another stellar population that may affect the appearance of the ChMs and likely has a connection to binary stars is the blue stragglers (BSs). In particular, we consider their evolved counterparts that lie close to the RGB. In Figure 7, we use blue symbols to represent the candidate BS stars of NGC 3201 in the $m_{F336W} - (m_{F275W} - m_{F814W})$ CMD. The objects marked with blue asterisks are possible BSs selected on the CMD that are evolving toward the RGB phase, which clearly displays lower $C_{F275W,F336W,F438W}$ values in the $m_{F336W} - C_{F275W,F336W,F438W}$ diagram (top right panel). The BSs in GCs are tightly linked to the cluster binary populations (Knigge et al. 2009). The BSs in open clusters themselves have a very high binary fraction (Mathieu & Geller 2009), and preliminary evidence suggests the same is true in NGC 3201 (Giesers et al. 2019). When we include the evolved BSs in the ChM (bottom panel of Figure 7), they populate a well-defined sequence on the blue extension of the 1G sequence. We conclude that, based on RVs and *s*-process element abundances, the three bluest 1G stars that we analyzed spectroscopically are binary systems. Some of them are possibly associated with the BS population of NGC 3201, as evolved BSs would contribute to the bluest extension of the 1G sequence in the ChM.

### 6.1. Noninteracting Binary Simulations

To investigate the effect of noninteracting binaries formed by pairs of 1G stars, we reproduce in Figure 8 five isochrones, I1—I5, with [Fe/H] = −1.50, [$\alpha$/Fe] = 0.4, and an age of

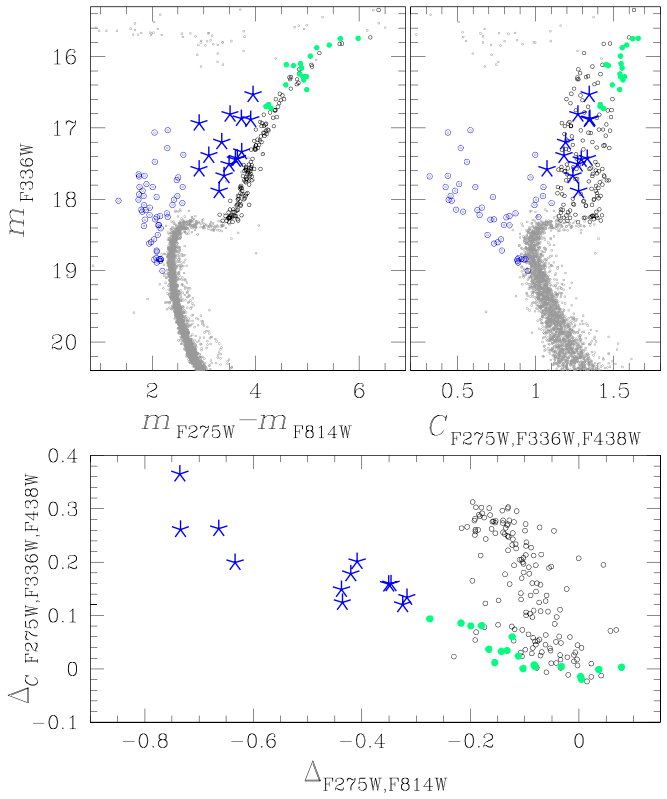


**Figure 7.** Top panels: $m_{F336W} - (m_{F275W} - m_{F814W})$ CMD (left) and $m_{F336W} - C_{F275W,F336W,F438W}$ diagram (right) of NGC 3201. Bottom panel: ChM of NGC 3201, similar to Figure 1 but extended to show the evolved BSs. In all panels, the green dots represent our analyzed spectroscopic targets, the open blue circles are the BSs, and the blue asterisks are the evolved BSs.

13 Gyr from Milone et al. (2018). These isochrones are constructed with a different combination of He, C, N, and O to represent the typical chemical pattern of different stellar populations in GCs. We used the isochrone I1, which correponds to the 1G, to generate a stellar population of 1G–1G binaries that we represent with black points in Figure 8.

The corresponding ChM plane of RGB stars for the five populations is shown in the right panel. Together with the five isochrones with different chemical abundances, we plot a population of simulated 1G–1G binaries (black points) constructed by assuming a flat distribution in the mass ratio ($q$). This test clearly demonstrates that binaries can contribute to the width of the 1G in the ChM. However, we find that the shift toward bluer $\Delta_{F275W,F814W}$ is dependent on the mass ratio, and only binaries with a large mass ratio ($q \gtrsim 0.8$) are able to provide a significant color spread.

To have a more direct comparison with the ChM of NGC 3201, in Figure 9, we superimpose on the observed map two simulated binary populations: (i) a population of binaries that account for the whole cluster (100% of binaries), with both the 1G–1G and the 2G–2G pairs (top panel); and (ii) a more realistic simulation, where the binary population fraction is 12.8%, as reported in Milone et al. (2012b) for the main-sequence binaries (bottom panel). In the latter, we assume that all of the binaries are 1G–1G pairs. Again, we find that the 1G–1G binaries can affect the elongation of the 1G on lower $\Delta_{F275W,F814W}$ values, but the observed binary fractions on the main sequence are not able to account for the relatively high number of stars observed on the bluer extention of the ChM.

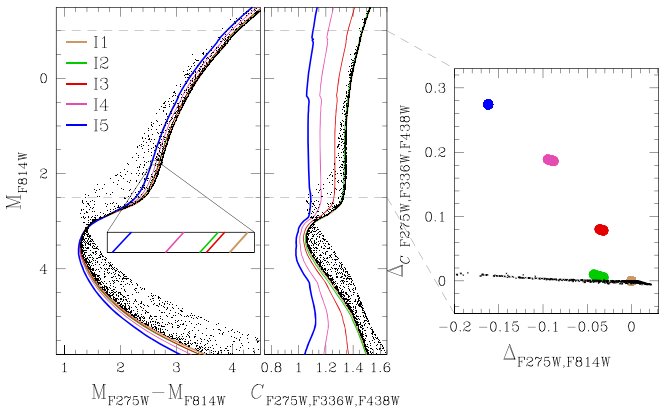


**Figure 8.** Left panels: simulated CMD, with five isochrones corresponding to different stellar populations with different He, C, N, and O. Here I1 is the isochrone corresponding to the first population; I2 has the same abundance of C, N, and O as I1 but different He; and in I3, I4, and I5, the abundances of He, C, N, and O have been varied to represent the second population chemical pattern. Right panel: location of the five different stellar simulated populations at a reference magnitude on the ChM plane. The black points are noninteracting binaries formed by pairs of I1–I1 stars. Binaries can contribute to the width of the 1G in the ChM, but only binaries with a large mass ratio ($q \gtrsim 0.8$) can provide a significant color spread.

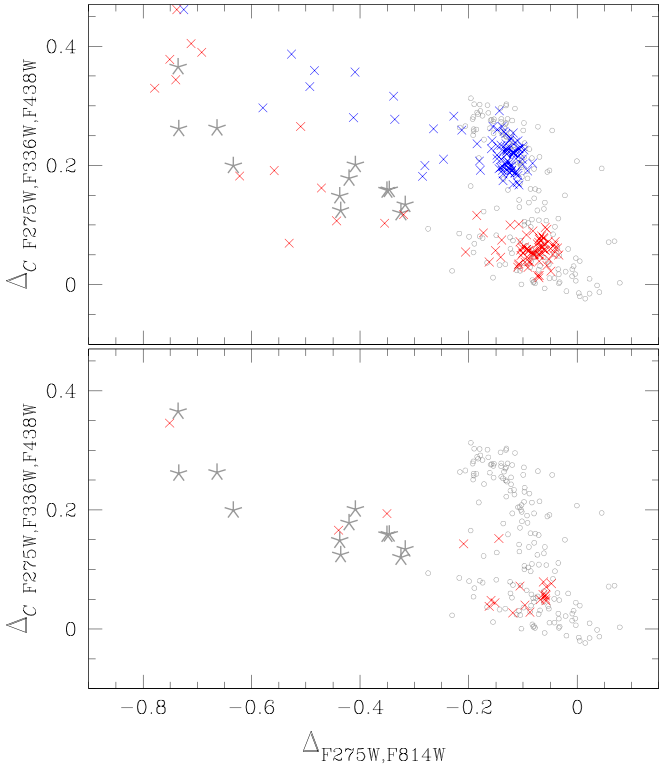


**Figure 9.** Observed ChM of NGC 3201 (gray symbols). The stars with extremely low $\Delta_{F275W,F814W}$ are plotted as gray asterisks. Superimposed on the observed ChM are simulations of binary stars: in the top panel, we have simulated a cluster with 100% of the binaries, both 1G–1G (red) and 2G–2G (blue); in the bottom panel, we have simulated 12.8% of the binaries, which is the observed fraction on the main sequence (Milone et al. 2012b), by assuming that all of them are 1G–1G binaries.

## 7. ChM and Abundance Pattern of 1G Stars

In the right panel of Figure 5, we show the [La/Fe] abundances as a function of the $\Delta_{F275W,F814W}$ axis of the ChM.

The three binary candidates are the stars with the lowest $\Delta_{F275W,F814W}$ values in our sample. As discussed in the previous section, this suggests that the stars with the lowest $\Delta_{F275W,F814W}$ on the map are likely associated with binaries and/or BSs, with no need to invoke chemical abundance variations like He enhancements.

However, our simulations suggest that we would need a high number of binaries at high $q$ to account for all of the stars in the 1G population. This requirement might suggest that some additional mechanism might be necesary to account for a range of ∼0.2 mag in $\Delta_{F275W,F814W}$ among 1G stars in NGC 3201, and similarly in many other GCs.

In Figure 5, the color code used is indicative of the Fe abundance. We immediately note that the stars with lower $\Delta_{F275W,F814W}$ also have lower iron, with star 27 ($\Delta_{F275W,F814W} = +0.0026$) and star 33 ($\Delta_{F275W,F814W} = -0.1231$) being the stars with the highest and lowest metallicity, respectively, giving a maximum range of 0.19 dex (neglecting the three binary candidates).

This result suggests that there is a small Fe variation among 1G stars in NGC 3201. By dividing our sample of 15 stars on the basis of the $\Delta_{F275W,F814W}$ value, we find that eight stars with $\Delta_{F275W,F814W} < -0.10$ have $\langle[Fe/H]\rangle = -1.53 \pm 0.02$, while the seven stars at higher $\Delta_{F275W,F814W}$ have $\langle[Fe/H]\rangle = -1.45 \pm 0.01$, a more than $2.5\sigma$ difference. This difference is smaller than that inferred for the blue and red RGB stars in the Type II GCs (Marino et al. 2019) and hardly detectable. Our relatively high-S/N and high-resolution UVES spectra for 15 stars allow us to still detect the difference at a $<3\sigma$ level. We also note that the dispersion associated with our [Fe/H] average abundance is comparable with the estimated error.

At this point, it is worth discussing the impact of non-LTE corrections on this result, which is based on LTE abundance analysis. We first note that, as amply discussed in Kovalev et al. (2019), non-LTE analysis changes the mean abundance ratios in clusters, but intracluster abundance dispersions should not be significantly affected. However, to test this, we derived the non-LTE corrections to our Fe I and Fe II spectral lines (Bergemann et al. 2012; Lind et al. 2012) by using the available online database (http://inspect-stars.com/). For this test, we use stars 69 and 82, which have similar atmospheric parameters (both from spectroscopy and photometry) but different $\Delta_{F275W,F814W}$, with star 82 having a higher derived [Fe/H]. We find that the non-LTE correction to apply to Fe I lines is +0.07 dex for both stars and does not change significantly from line to line. The Fe II abundances decrease by −0.01, again in both stars. Using non-LTE Fe abundances for the determination of the atmospheric parameters only marginally changes the spectroscopic temperature, by +30–40 K in both stars. From this test, it is clear that, although non-LTE abundances are more realistic, in our sample of stars, the corrections are systematic and similar in all stars. The difference in [Fe/H] between the two stars is kept unchanged.

Figure 10 shows [Fe/H] as a function of $\Delta_{F275W,F814W}$. Excluding the three binary candidates, we get a positive correlation (slope = 0.50) with a Spearman correlation coefficient $r = 0.68$. We have derived the significance of the correlation from a Monte Carlo of 1000 realizations of our data set composed of 15 stars. In each realization, we have assumed the observed $\Delta_{F275W,F814W}$ and a uniform Fe abundance with the associated error estimates of Table 7 and derived the slope. We have calculated the fraction ($f$) of realizations where the slope is equal to or higher than the observed one and assumed this value as the probability that the slope is due to randomness. For [Fe/H], we get a slope higher than the observed value in 2.2% of the simulations (see Table 8).

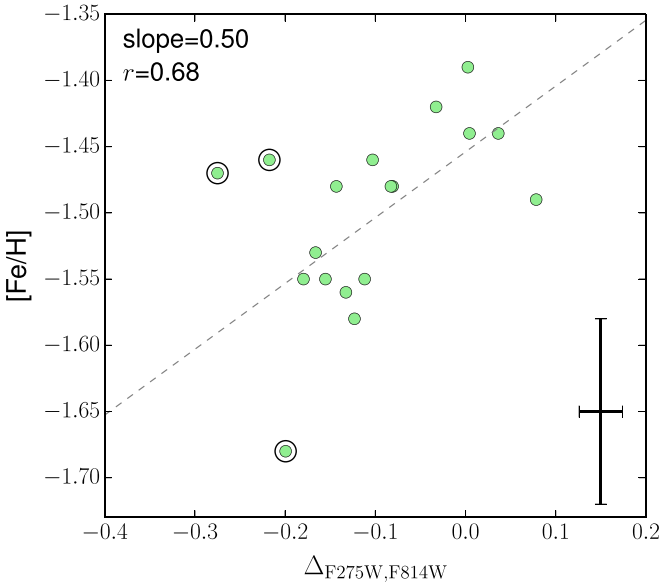


**Figure 10.** Chemical abundances [Fe/H] as a function of $\Delta_{F275W,F814W}$ values on the ChM of NGC 3201. The dashed line is the least-squares linear fit to the data (neglecting the three binary candidates). The slope and Spearman correlation coefficient ($r$) are highlighted in the top left corner.

Figure 11 represents the Spearman correlation for each $\log\epsilon(X)$ abundance as a function of the $\Delta_{F275W,F814W}$ and $\Delta_{C\ F275W,F336W,F438W}$ value on the ChM of NGC 3201. The obtained correlation values between $\Delta_{F275W,F814W}$ and the $\log\epsilon$ abundances are listed in Table 8, together with the associated $f$. Although not all of the correlations are significant, given the relatively small sample size, clearly all of the abundances appear to be positively correlated with $\Delta_{F275W,F814W}$. We regard the negative correlation with $\Delta_{C\ F275W,F336W,F438W}$ as simply due to the fact that our stars with low $\Delta_{F275W,F814W}$ have slightly higher $\Delta_{C\ F275W,F336W,F438W}$ (see Figure 1). However, the presence of a general correlation between each absolute abundance and the $\Delta_{F275W,F814W}$ corroborates the presence of a small spread in the overall metallicity among 1G stars in NGC 3201.

A quick look at the spectra further supports this finding. As an example, in Figure 12, we show the portion of two spectra, including some Fe and Ca analyzed spectral features, for two stars with different $\Delta_{F275W,F814W}$ and similar atmospheric parameters. We note that the two chosen stars also have very similar atmospheric parameters from photometry. Overall, the spectral features of the star at higher $\Delta_{F275W,F814W}$ look consistent with higher metals.

As first suggested by Milone et al. (2015, 2017), a variation in the He content intrinsic to the 1G stars is qualitatively able to account for the $\Delta_{F275W,F814W}$ spread. However, such a variation in He should be high, at a level of $\Delta Y \sim 0.08$–$0.10$, which is difficult to achieve without any corresponding enhancement in other chemical species, such as N and Na, and depletion in O (Marino et al. 2019). As discussed in Section 5 our analyzed stars in NGC 3201 have similar [O/Fe] and [Na/Fe] abundances.

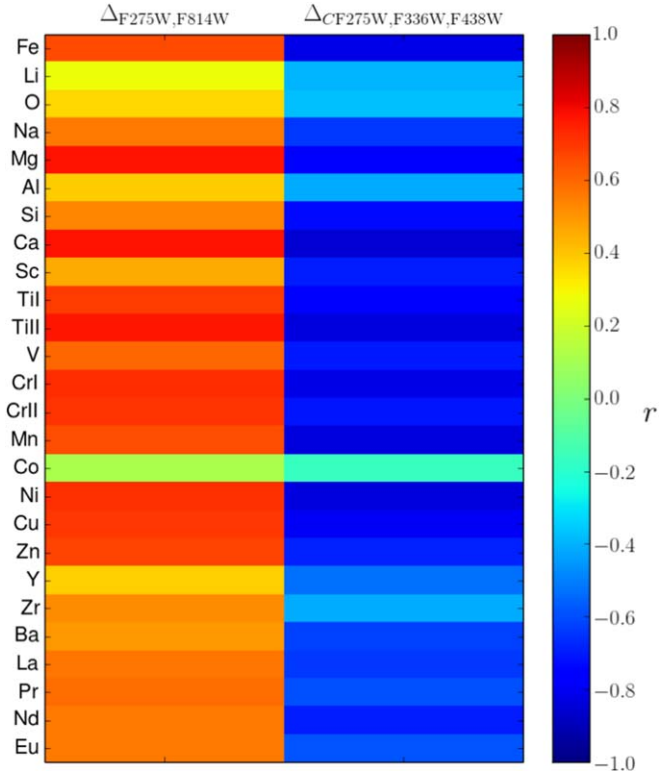


**Figure 11.** Chemical abundances log $\epsilon$(X) as a function of $\Delta_{F275W,F814W}$ and $\Delta_{C\ F275W,F336W,F438W}$ values on the ChM of NGC 3201. For Li and Na, we use the non-LTE abundances. The color code is indicative of the Spearman correlation coefficient ($r$). The significance of these correlations is listed in Table 8.

**Table 8**
Spearman Correlation Coefficient ($r$) for Each log $\epsilon$(X) Abundance as a Function of $\Delta_{F275W,F814W}$ and Probability That the Corresponding Slope is Due to Randomness ($f$)

| Element | $r$ | $f$ (%) |
|---|---|---|
| Fe | 0.68 | 2.2 |
| $Li_{non-LTE}$ | 0.35 | 27.6 |
| O | 0.38 | 33.1 |
| $Na_{non-LTE}$ | 0.56 | 3.1 |
| Mg | 0.70 | 3.7 |
| Al | 0.37 | 37.6 |
| Si | 0.51 | 9.9 |
| Ca | 0.75 | 0.0 |
| Sc II | 0.47 | 8.2 |
| Ti I | 0.68 | 0.0 |
| Ti II | 0.75 | 2.2 |
| V | 0.57 | 3.5 |
| Cr I | 0.68 | 0.3 |
| Cr II | 0.61 | 0.5 |
| Mn | 0.63 | 0.2 |
| Co | 0.09 | 40.0 |
| Ni | 0.67 | 0.0 |
| Cu | 0.66 | 1.0 |
| Zn | 0.65 | 1.0 |
| Y II | 0.37 | 4.8 |
| Zr II | 0.38 | 25.2 |
| Ba II | 0.55 | 18.7 |
| La II | 0.60 | 2.9 |
| Pr II | 0.57 | 15.5 |
| Nd II | 0.52 | 10.1 |
| Eu II | 0.63 | 4.1 |

Assuming the working hypothesis that an He variation exists among our stars, we would expect a difference in the structure of a model atmosphere between an He-normal and an He-rich star (Stromgren et al. 1982). Such a difference would translate into a different surface gravity, which is expected to be small (<0.10 dex). Looking at the impact of a variation in log $g$ by 0.20 dex on the chemical abundances, it is unlikely that such variations in log $g$ introduced by possible He variations are responsible for the abundance variations we find.

As widely discussed in Yong et al. (2013a), a second effect of possible He variations is that for a fixed mass fraction of metals ($Z$), a change in the helium mass fraction ($Y$) will directly affect the hydrogen mass fraction ($X$) such that the metal-to-hydrogen ratio, $Z/X$, will change with the helium mass fraction, since $X + Y + Z = 1$. Hence, if stars in a GC have a constant $Z$, an He-rich star will appear to be slightly more metal-rich than an He-normal star. In this context, by using spectra of excellent quality, Yong et al. (2013a) found variations at a level of a few hundredths of a dex in the absolute chemical abundances of giants in NGC 6752, positively correlated with Na (a tracer of He).[13]

For a fixed $Z$, in the case of a variation in $Y$ of 0.10 (the one predicted to account for the $\Delta_{F275W,F814W}$ extention in NGC 3201), [$Z/H$] would change by ∼0.06 dex, which is slightly lower than the range we find in the cluster. However, as a pure He enhancement shifts stars toward lower $\Delta_{F275W,F814W}$ values (Milone et al. 2015; Marino et al. 2019), this second explanation can be ruled out for our 1G stars in NGC 3201, as the stars that should be enhanced in He (at lower $\Delta_{F275W,F814W}$) are metal-poorer. Clearly, they are located on the blue side of the RGB and ChM, reinforcing the idea that at least the bluest side of 1G in the ChM is populated by binaries and/or evolved BSs.

On the other hand, if we assume that all of the metal-poorer and bluest stars are indeed binaries, we expect that the sum of the spectra of the two binary components is reflected in some variation in the line-flux/continuum ratio. Depending on the brightness of the two stars, these effects might not be negligible and can affect the derived atmospheric parameters. To qualitatively investigate this issue, we have simulated some spectra with the SYNTHE routine in the ATLAS code (Kurucz 2009). For this purpose, we considered a bright giant star with ($T_{eff}$/log $g$/[A/H]/$\xi_t$) = (4650 K/1.60/−1.50/2.00 km s$^{-1}$) and two less luminous stars, namely a fainter giant (5000 K/2.53/−1.50/2.00 km s$^{-1}$) and a subgiant (6000 K/4.00/−1.50/2.00 km s$^{-1}$). By summing the flux of the bright giant and subgiant, the combined spectrum is almost identical to the giant spectrum. However, the sum of the two giants results in an emerging spectrum that is consistent with either lower overall metallicity (by 0.06 dex) or higher $T_{eff}$ (by 50 K). Binaries where the two components are both giants but with different luminosities can potentially explain the lower metals in the bluest 1G stars; however, as far as we know, it is unlikely to have as many giant pairs as the bluer 1G stars (Milone et al. 2012b).

[13] For NGC 6752, high-precision photometry infers a $\Delta Y$ of the order of a few hundredths (Milone et al. 2018), not enough to entirely account for the observed abundance correlations derived in Yong et al. (2013a). Yong and coworkers suggested that a combination of He variations and inhomogeneous chemical evolution in the protocluster environment could account for the chemical abundance variations.

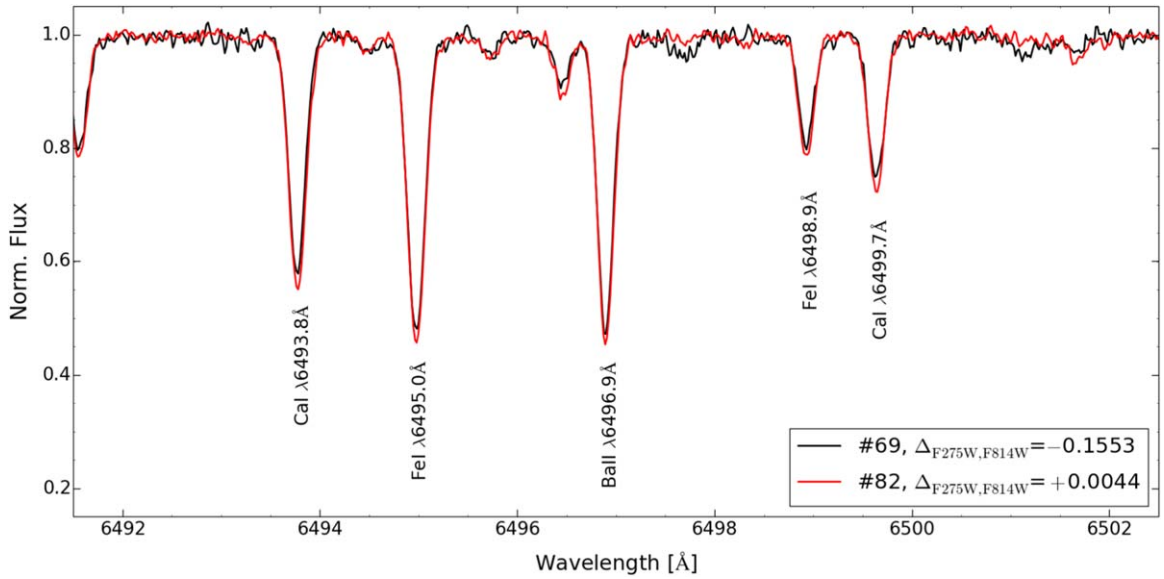


**Figure 12.** Examples of two portions of spectra including some Fe and Ca analyzed spectral features, plus the Ba line 6496.9 Å. The two represented spectra are for two stars with similar atmospheric parameters, namely stars 69 ($(T_{\rm eff}/\log g/[{\rm A/H}]/\xi_{\rm t}) = (4850\ {\rm K}/2.00/-1.55/1.48\ {\rm km\ s^{-1}})$) and 82 ($(T_{\rm eff}/\log g/[{\rm A/H}]/\xi_{\rm t}) = (4860\ {\rm K}/2.05/-1.44/1.49\ {\rm km\ s^{-1}})$) but different $\Delta_{\rm F275W,F814W}$ values. Overall, the spectral features of star 82, with higher $\Delta_{\rm F275W,F814W}$, are deeper.

## 8. Discussion and Conclusions

We have presented a high-resolution chemical abundance analysis of 18 stars of the GC NGC 3201. The 18 stars have all been selected to belong to the 1G stellar population, as defined in the ChM diagnostic tool in Milone et al. (2017). Although located on the 1G ChM sequence, our targets span a large range in the $\Delta_{\rm F275W,F814W}$ axis.

Overall, we have found that the abundances relative to Fe of all of the inferred species are consistent with a uniform chemical composition relative to Fe. Specifically, the stars have similar O and Na, consistent with the 1G chemical abundances. This finding confirms previous results showing that the elongation in $\Delta_{\rm F275W,F814W}$ of the 1G in GCs is not related to the common light-element (anti)correlations (Cabrera-Ziri et al. 2019; Marino et al. 2019). The constancy in light elements makes it hard to believe that the stars with lower $\Delta_{\rm F275W,F814W}$ have higher He abundances, as tentatively suggested by Milone et al. (2015).

The three stars with the lowest $\Delta_{\rm F275W,F814W}$ values in the sample are binary candidates (see Figure 5). Two of these stars have higher RV rms over an observation time of a few months than the bulk of our stars. One star (star 93) also shows extremely high *s*-process element abundances. A high *s*-element abundance is associated with long-period, single-lined spectroscopic binary systems (McClure 1989). The unseen companion was a low-mass AGB star that transferred processed material to the surviving visible star. A third star shows higher *s*-element abundances, although not as extreme as star 93, but its rms in RVs is similar to the bulk of stars. This latter star, however, has a relatively short observational time coverage of 3 days.

These results strongly suggest that the stars with the lower $\Delta_{\rm F275W,F814W}$ values on the ChM, specifically those with $\Delta_{\rm F275W,F814W} \lesssim -0.18$ in NGC 3201, are binaries. It is interesting to note that barium- and CH-type stars generally form via wind mass transfer in fairly wide binaries (Jorissen et al. 1998). Such wide binaries are not likely to survive in a GC because of dynamical interactions, which suggests that the two *s*-rich stars either may not be in binary systems today or formed via Roche Lobe overflow, which can lead to tighter, shorter period binaries more likely to survive in a GC.

The observed distribution in $\Delta_{\rm F275W,F814W}$ is consistent with simulations of noninteracting binaries (presented in Section 6.1) formed by two stars belonging to the 1G population, which predicts these objects on lower $\Delta_{\rm F275W,F814W}$ values. The fact that 2G stars in the ChM do not show a large spread in $\Delta_{\rm F275W,F814W}$, as the 1G does, might support the idea of a predominance of 1G–1G binaries in GCs (Lucatello et al. 2015). Furthermore, we note that the BS population accounts for the bluest stars in the elongated 1G population observed on the ChM.

Excluding the three binary candidates, we found a small variation in the overall metallicity in the remaining 15 giants. Here [Fe/H] has a range of the order of ∼0.1 dex, which is correlated with the $\Delta_{\rm F275W,F814W}$ value. The absolute abundances of the other analyzed elements follow the same variation of Fe, keeping constant the abundance ratios relative to Fe. We exclude the possibility that this small variation in metals is introduced by a change in helium (Y) and a consequent change in *Z*/*X*, as in this case, we would expect the opposite trend with the $\Delta_{\rm F275W,F814W}$ values.

We can interpret the observed small change in the overall metallicity either as a hint of internal variations among 1G stars or as an artifact of binarity. In the first case, we have to account for an inhomogeneity in the primordial cloud from which the GC formed. In this context, we note that, when data of excellent quality are analyzed, very small internal variations in metals are also found in open clusters (Liu et al. 2016). On the other hand, our simulated spectra of binaries suggest that a giant–giant pair (not identical) spectrum is consistent with higher temperature and/or metallicity, as is the one we find. Previous work on the binary fraction of NGC 3201, however, does not support such a high number of binaries as the one required to account for the observed elongated 1G (Milone et al. 2012b).

We conclude that binarity surely contributes to the elongation of the 1G in NGC 3201. On the other hand, only binaries with $q \gtrsim 0.8$ can produce a sizable shift toward low

$\Delta_{F275W,F814W}$ values. As an additional mechanism, a small inhomogeneity in metals can account for some of the spread among 1G stars in the map. Helium variations, while able to theoretically produce the observed elongation along the 1G on the ChM, seem unlikely.

The authors warmly thank the anonymous referee for very insightful discussion. This work has received funding from the European Research Council (ERC) under the European Union's Horizon 2020 research innovation program (grant agreement ERC-StG 2016, No. 716082 "GALFOR," PI: Milone) and the European Union's Horizon 2020 research and innovation program under Marie Skłodowska-Curie grant agreement No. 797100. A.P.M. and M.T. acknowledge support from MIUR through the FARE project R164RM93XW "SEMPLICE." H.J. acknowledges support by the Australian Research Council through the Discovery Project DP150100862.

*Software:* ATLAS code (Kurucz 2009), MOOG code (Sneden 1973), EsoReflex interface (Ballester et al. 2000), ESO MOLECFIT tool (Smette et al. 2014; Kausch et al. 2014).

## ORCID iDs

A. F. Marino https://orcid.org/0000-0002-1276-5487
A. P. Milone https://orcid.org/0000-0001-7506-930X
A. Renzini https://orcid.org/0000-0002-7093-7355
G. Cordoni https://orcid.org/0000-0002-7690-7683
F. D'Antona https://orcid.org/0000-0003-4697-0945
H. Jerjen https://orcid.org/0000-0003-4624-9592
A. Karakas https://orcid.org/0000-0002-3625-6951
E. Lagioia https://orcid.org/0000-0003-1713-0082
G. Piotto https://orcid.org/0000-0002-9937-6387

## References

Alonso, A., Arribas, S., & Martínez-Roger, C. 1999, A&AS, 140, 261
Anderson, J., Sarajedini, A., Bedin, L. R., et al. 2008, AJ, 135, 2055
Ballester, P., Modigliani, A., Boitquin, O., et al. 2000, Msngr, 101, 31
Bergemann, M., Lind, K., Collet, R., Magic, Z., & Asplund, M. 2012, MNRAS, 427, 27
Cabrera-Ziri, I., Lardo, C., & Mucciarelli, A. 2019, MNRAS, 485, 4128
Carretta, E., Bragaglia, A., Gratton, R. G., et al. 2009, A&A, 505, 117
Castelli, F., & Kurucz, R. L. 2004, arXiv:astro-ph/0405087
Cohen, J. G. 1978, ApJ, 223, 487
Cristallo, S., Straniero, O., Gallino, R., et al. 2009, ApJ, 696, 797
D'Antona, F., Vesperini, E., D'Ercole, A., et al. 2016, MNRAS, 458, 2122
Dekker, H., D'Odorico, S., Kaufer, A., et al. 2000, Proc. SPIE., 4008, 534
Dias, B., Araya, I., Nogueira-Cavalcante, J. P., et al. 2018, A&A, 614, A146
Fishlock, C. K., Karakas, A. I., Lugaro, M., et al. 2014, ApJ, 797, 44
Frank, M. J., Koch, A., Feltzing, S., et al. 2015, A&A, 581, A72
Gallino, R., Arlandini, C., Busso, M., et al. 1998, ApJ, 497, 388
Giesers, B., Kamann, S., Dreizler, S., et al. 2019, arXiv:1909.04050
Gratton, R. G., Carretta, E., & Bragaglia, A. 2012, A&ARv, 20, 50
Harding, G. A. 1962, Obs, 82, 205
Harris, W. E. 2010, arXiv:1012.3224
Hobbs, L. M., & Thorburn, J. A. 1997, ApJ, 491, 772
Jorissen, A., Van Eck, S., Mayor, M., et al. 1998, A&A, 332, 877
Karakas, A. I., & Lattanzio, J. C. 2014, PASA, 31, e030
Kausch, W., Noll, S., Smette, A., et al. 2014, in ASP Conf. Ser. 485, adass XXIII, ed. N. Manset & P. Forshay (San Francisco, CA: ASP), 403
Knigge, C., Leigh, N., & Sills, A. 2009, Natur, 457, 288
Kovalev, M., Bergemann, M., Ting, Y.-S., et al. 2019, A&A, 628, A54
Kurucz, R. L. 2009, in AIP Conf. Ser. 1171, Recent Directions in Astrophysical Quantitative Spectroscopy and Radiation Hydrodynamics (Melville, NY: AIP), 43
Lawler, J. E., Bonvallet, G., & Sneden, C. 2001a, ApJ, 556, 452
Lawler, J. E., Wickliffe, M. E., den Hartog, E. A., & Sneden, C. 2001b, ApJ, 563, 1075
Lind, K., Asplund, M., & Barklem, P. S. 2009a, A&A, 503, 541
Lind, K., Asplund, M., Barklem, P. S., et al. 2011, A&A, 528, A103
Lind, K., Bergemann, M., & Asplund, M. 2012, MNRAS, 427, 50
Lind, K., Primas, F., Charbonnel, C., Grundahl, F., & Asplund, M. 2009b, A&A, 503, 545
Liu, F., Asplund, M., Yong, D., et al. 2016, MNRAS, 463, 696
Lucatello, S., Sollima, A., Gratton, R., et al. 2015, A&A, 584, A52
Marino, A. F., Milone, A. P., Karakas, A. I., et al. 2015, MNRAS, 450, 815
Marino, A. F., Milone, A. P., Piotto, G., et al. 2009, A&A, 505, 1099
Marino, A. F., Milone, A. P., Renzini, A., et al. 2019, MNRAS, 487, 3815
Marino, A. F., Villanova, S., Piotto, G., et al. 2008, A&A, 490, 625
Mathieu, R. D., & Geller, A. M. 2009, Natur, 462, 1032
McClure, R. D. 1989, IAU Colloq. 106 in Evolution of Peculiar Red Giant Stars, ed. H.R. Johnson & B. Zuckerman (Cambridge: Cambridge Univ. Press), 196
McWilliam, A. 1998, AJ, 115, 1640
Milone, A. P., Marino, A. F., Piotto, G., et al. 2015, MNRAS, 447, 927
Milone, A. P., Marino, A. F., Renzini, A., et al. 2018, MNRAS, 481, 5098
Milone, A. P., Piotto, G., Bedin, L. R., et al. 2012a, ApJ, 744, 58
Milone, A. P., Piotto, G., Bedin, L. R., et al. 2012b, A&A, 540, A16
Milone, A. P., Piotto, G., Renzini, A., et al. 2017, MNRAS, 464, 3636
Nataf, D. M., Gould, A. P., Pinsonneault, M. H., et al. 2013, ApJ, 766, 77
Norris, J. E., Yong, D., Gilmore, G., & Wyse, R. F. G. 2010, ApJ, 711, 350
Osborn, W. 1971, Obs, 91, 223
Pasquini, L., Avila, G., Allaert, E., et al. 2000, Proc. SPIE, 4008, 129
Piatti, A. E., & Koch, A. 2018, ApJ, 867, 8
Piotto, G., Milone, A. P., Bedin, L. R., et al. 2015, AJ, 149, 91
Popper, D. M. 1947, ApJ, 105, 204
Smette, A., et al. 2014, submitted
Sneden, C. 1973, ApJ, 184, 839
Stromgren, B., Gustafsson, B., & Olsen, E. H. 1982, PASP, 94, 5
Tailo, M., D'Antona, F., Caloi, V., et al. 2019, MNRAS, 486, 5895
Yong, D., & Grundahl, F. 2008, ApJL, 672, L29
Yong, D., Grundahl, F., Johnson, J. A., et al. 2008, ApJ, 684, 1159
Yong, D., Meléndez, J., Grundahl, F., et al. 2013a, MNRAS, 434, 3542
Yong, D., Norris, J. E., Bessell, M. S., et al. 2013b, ApJ, 762, 26